

ALLSMOG: an APEX Low-redshift Legacy Survey for MOlecular Gas

I – molecular gas scaling relations, and the effect of the CO/H₂ conversion factor

M. S. Bothwell^{1,2*}, J. Wagg^{1,2,3,4}, C. Cicone^{1,2}, R. Maiolino^{1,2}, P. Møller⁴,
M. Aravena^{4,5}, C. De Breuck⁶, Y. Peng^{1,2}, D. Espada^{7,8,9}, J. A. Hodge¹⁰,
C. M. V. Impellizzeri^{7,10}, S. Martín¹¹, D. Riechers¹², F. Walter¹³

¹*Cavendish Laboratory, University of Cambridge, 19 J.J. Thomson Avenue, Cambridge, CB3 0HE, UK*

²*Kavli Institute for Cosmology, University of Cambridge, Madingley Road, Cambridge CB3 0HA, UK*

³*Square Kilometre Array Organisation, Jodrell Bank Observatory, Lower Withington, Macclesfield, Cheshire SK11 9DL, UK*

⁴*European Southern Observatory, Alonso de Córdova 3107, Vitacura, Casilla 19001, Santiago 19, Chile*

⁵*Núcleo de Astronomía, Facultad de Ingeniería, Universidad Diego Portales, Av. Ejército 441, Santiago, Chile*

⁶*European Southern Observatory, Karl Schwarzschild Strae 2, 85748 Garching bei München, Germany*

⁷*Joint ALMA Observatory, Alonso de Cordova 3107, Vitacura, 763-0355, Santiago, Chile*

⁸*National Astronomical Observatory of Japan (NAOJ), 2-21-1 Osawa, Mitaka, 181-8588, Tokyo, Japan*

⁹*The Graduate University for Advanced Studies (SOKENDAI), 2-21-1 Osawa, Mitaka, 181-8588, Tokyo, Japan*

¹⁰*National Radio Astronomy Observatory, 520 Edgemont Rd, Charlottesville, VA, 22903, USA*

¹¹*Institut de Radio Astronomie Millimétrique, 300 rue de la Piscine, Dom. Univ., 38406, St. Martin d'Hères, France*

¹²*Department of Astronomy, 220 Space Science Building, Cornell University, Ithaca, NY, 14853, USA*

¹³*Max Planck Institut für Astronomie, Königstuhl 17, 69117 Heidelberg, Germany*

Accepted —. Received — in original form —

ABSTRACT

We present ALLSMOG, the APEX Low-redshift Legacy Survey for MOlecular Gas. ALLSMOG is a survey designed to observe the CO(2–1) emission line with the APEX telescope, in a sample of local galaxies ($0.01 < z < 0.03$), with stellar masses in the range $8.5 < \log(M_*/M_\odot) < 10$. This paper is a data release and initial analysis of the first two semesters of observations, consisting of 42 galaxies observed in CO(2–1).

By combining these new CO(2–1) emission line data with archival HI data and SDSS optical spectroscopy, we compile a sample of low-mass galaxies with well defined molecular gas masses, atomic gas masses, and gas-phase metallicities. We explore scaling relations of gas fraction and gas consumption timescale, and test the extent to which our findings are dependent on a varying CO/H₂ conversion factor. We find an increase in the H₂/HI mass ratio with stellar mass which closely matches semi-analytic predictions. We find a mean molecular gas fraction for ALLSMOG galaxies of $M_{\text{H}_2}/M_* = (0.09 - 0.13)$, which decreases with stellar mass. This decrease in total gas fraction with stellar mass is in excess of some model predictions at low stellar masses. We measure a mean molecular gas consumption timescale for ALLSMOG galaxies of 0.4–0.7 Gyr. We also confirm the non-universality of the molecular gas consumption timescale, which varies (with stellar mass) from ~ 100 Myr to ~ 2 Gyr. Importantly, we find that the trends in the H₂/HI mass ratio, gas fraction, and the non-universal molecular gas consumption timescale are all robust to a range of recent metallicity-dependent CO/H₂ conversion factors.

Key words: galaxies: evolution – galaxies: formation – galaxies: abundances – galaxies: statistics

arXiv:1409.4764v1 [astro-ph.GA] 16 Sep 2014

1 INTRODUCTION

The cold phase of the interstellar medium (ISM) is a central ingredient in the galaxy evolution process. In the early Universe, rarified cold gas rained down into the potential wells of primordial dark matter haloes, but it was not until the gas collapsed and fragmented, forming dense molecular clouds, that star formation could begin. In the present-day Universe stars form exclusively in the dense cores of molecular clouds, and, as such, molecular gas acts as the critical precursor for star formation.

In spite of the importance of molecular gas in driving star formation, there remain many outstanding problems to be addressed by extragalactic surveys. While modern optical galaxy surveys boast sample sizes into the millions, and the latest surveys for extragalactic *atomic* gas (in the form of H I) have many tens of thousands of members, typical surveys for molecular gas generally detect, at most, on the order of a few hundred galaxies. A primary difficulty in observing molecular hydrogen is its lack of a permanent dipole moment, making H₂ exceptionally faint in emission, directly detectable in only a handful of very local sources. Combined with the fact that the IR emission lines of H₂ are emitted by warm gas (rather than tracing the bulk of the cold molecular ISM), this makes a direct detection of H₂ an utterly impractical strategy for a large extragalactic survey.

The traditional approach to overcoming this issue is to use a ‘tracer’ molecule, which is easily observable and can be assumed to be approximately co-spatial with cold H₂. By far, the most popular choice of tracer molecule in use is carbon monoxide (¹²C¹⁶O – simply ‘CO’ hereafter)¹. CO makes for an ideal tracer molecule – it has a low excitation energy, and exhibits bright emission lines at approximately integer multiples of 115.27 GHz, the two lowest transitions of which fall conveniently into the mm-wavelength atmospheric windows. CO is therefore detectable across an enormous distance range, from the very local Universe out to $z > 5$ (Weiß et al. 2013; for a recent review see Carilli & Walter 2013).

The inherent difficulty in using CO to trace molecular gas, of course, is that *by mass* it represents only a tiny fraction of the molecular ISM (which is predominantly composed of molecular hydrogen and helium). Converting from a CO luminosity to a total mass of molecular gas, therefore, requires the use of a ‘conversion factor’ (often denoted ‘ α_{CO} ’), which encodes information about the fraction of CO relative to H₂. There has been a vast amount of work over the last few decades dedicated to empirically measuring, and theoretically modelling, α_{CO} (see Bolatto et al. 2013 for a recent review) for individual molecular clouds. By making a few assumptions (such as a population of isolated and virialised molecular clouds), it is possible to derive a *global* α_{CO} , applicable – in an average sense – to entire galaxies.

This assumed value of α_{CO} is not a universal constant however – the value for any specific galaxy may be higher or lower than the average value estimated for the Milky Way, depending on the specific conditions within the ISM. It is now generally accepted that the primary factor driving galaxy-to-galaxy variations in α_{CO} is the metal abundance

of the ISM. A high abundance of metals in a molecular cloud results in more dust, which can shield CO from photodissociation. At lower metallicities, the region of a molecular cloud capable of forming CO molecules shrinks further and further into the dense core of the cloud. As such, a molecular gas cloud will produce less and less CO emission (for a given H₂ mass) as metallicity is decreased. This holds true when considering the integrated properties of galaxies – galaxies with lower gas-phase metallicities require higher values of α_{CO} in order to accurately derive their molecular gas masses (e.g., Genzel et al. 2011; Schruba et al. 2011; Narayanan et al. 2012).

This metallicity-dependence of α_{CO} may have limited extragalactic CO surveys in two ways. Firstly, due to the strong link between metallicity and stellar mass (e.g. Tremonti et al. 2004), molecular gas becomes increasingly difficult to detect in low mass galaxies. As such, most large surveys for molecular gas have been preferentially targeted towards samples at high stellar masses, while the molecular gas content of galaxies with low stellar masses, $M_* \lesssim 10^{10} M_{\odot}$ – a group which contains much of the molecular gas in the present day Universe (Keres et al. 2003) – remains comparatively poorly explored. The second difficulty is that without accurate gas-phase metallicities, molecular gas observations are difficult to interpret, necessitating the unphysical assumption of a constant α_{CO} which can lead to underlying trends being obscured or biased.

There have been a number of surveys undertaken to detect molecular gas, both locally and in the high-redshift Universe. Locally, observations tend to focus on lower- J transitions of CO in samples of massive ‘main sequence’ galaxies (Saintonge et al. 2011; Boselli et al. 2014; though see Leroy et al. 2005 for a smaller sample of low-mass galaxies), whereas gas observations at high redshift have, until recently, concentrated on higher- J observations of bright, starburst galaxies (e.g., Greve et al. 2005; Tacconi et al. 2006; Bothwell et al. 2010; Bothwell et al. 2013; for a recent review see Carilli & Walter 2013 and references therein)².

In recent years, there has been an effort to substantially increase the statistics of low-redshift molecular gas observations by means of large dedicated surveys: two such surveys are COLDGASS (the CO Legacy Database for the Galaxy Evolution Explorer (GALEX) Arecibo Sloan Digital Sky Survey (SDSS) Survey), and the Herschel Reference Survey. COLDGASS (Saintonge et al. 2011) is the molecular gas extension of the H I-based Galex-Arecibo SDSS survey ‘GASS’ (Catinella et al. 2010). COLDGASS is designed to survey molecular gas in nearby massive ($M_* > 10^{10} M_{\odot}$) galaxies, selected to have both SDSS and GALEX UV coverage. COLDGASS has successfully explored molecular gas scaling relations and gas consumption timescales at high stellar masses, finding (amongst other results) strong connections between the gas content and galaxy colour/morphology, and a non-universal molecular gas depletion timescale (Saintonge

¹ Using dust – observable via the far-IR continuum – as a gas tracer is also becoming popular; see Santini et al. (2014); Scoville et al. (2014).

² Technological advances have improved both of these shortcomings, however, with CO observations of high- z ‘main sequence’ galaxies being undertaken (Tacconi et al. 2013), as well as low- J observations at high- z (i.e., Ivison et al. 2011; Riechers et al. 2011) enabled by the addition of (26.5 to 40 GHz) Ka-band receivers on sensitive telescopes like the Karl G. Jansky Very Large Array (VLA).

et al. 2011). The Herschel Reference Survey (HRS hereafter; Boselli et al. 2010) is one program designed to start overcoming the bias towards high stellar masses. Boselli et al. (2014) obtained new molecular gas observations for 59 galaxies (and archival CO data for a further 166), with stellar masses as low as $10^9 M_{\odot}$, and explored a variety of scaling relations in this low stellar mass regime (Boselli et al. 2014). Using a H-band-dependent α_{CO} , Boselli et al. (2014) find that several scaling relations (including the molecular gas consumption timescale and the H_2/HI ratio) become statistically insignificant, or even disappear completely, when using this varying α_{CO} .

Mindful of the bias in molecular gas surveys towards samples of massive galaxies, we designed ALLSMOG, the Apex Large Legacy survey for MOlecular Gas. The ALLSMOG survey aims to explore molecular gas scaling relations, gas fractions, atomic/molecular gas ratios, and gas consumption timescales in a sample of ‘normal’ low mass local galaxies, with well-defined metallicities and stellar masses in the range $8.5 < \log(M_*/M_{\odot}) < 10$. Requiring a well-defined metallicity for inclusion in the ALLSMOG sample will ensure that it is possible to explore the effect of a variety of metallicity-dependent CO/H_2 conversion factors on any derived scaling relations, and – critically – identify the correlations that persist independent of the choice of conversion factor.

ALLSMOG is an APEX large program, being awarded 300 hours over 4 semesters, and is due to be completed in 2015. To date, the ALLSMOG program is $\sim 40\%$ complete after two semesters of observing, and has obtained $\text{CO}(2-1)$ observations for a total of 42 galaxies. This paper presents a data release and analysis of this first $\sim 40\%$ of our sample. The ALLSMOG survey was intended as a legacy survey for molecular gas in low-mass galaxies – as such, all reduced spectra have been made publicly available to the community, and can be accessed at www.mrao.cam.ac.uk/ALLSMOG.

Throughout this work, we have assumed a standard flat Λ -CDM cosmology with $H_0 = 70 \text{ km}^{-1} \text{ s}^{-1} \text{ Mpc}$.

2 SAMPLE SELECTION

ALLSMOG is designed to survey molecular gas in local galaxies with stellar masses $M_* < 10^{10} M_{\odot}$ – a mass range that is poorly explored by existing molecular gas surveys. We opted to survey the $\text{CO}(2-1)$ emission line, as it traces the cold molecular reservoir essentially as effectively as the $\text{CO}(1-0)$ line, while benefiting from a far higher expected flux density.

Our survey takes advantage of the enormous wealth of photometric and spectroscopic data made public as part of the SDSS data release 7. The basic SDSS DR7 data have been analysed by groups at the Max-Planck-Institut für Astrophysik (MPA) and JHU to produce catalogues³ with derived physical properties (stellar masses, star-formation rates, metallicities, etc.), which are briefly described in §3 below. The SDSS stellar masses are derived based on fitting described in Kauffmann et al. (2003), and star formation

rates are based on methods detailed in Brinchmann et al. (2004).

To assemble the ALLSMOG survey catalogue, we make cuts to the parent sample of the MPA-JHU catalogue to include galaxies:

- (i) with stellar masses, $8.5 < \log(M_*/M_{\odot}) < 10.0$;
- (ii) with declinations less than $+10^\circ$ (to ensure that they are observable with APEX at high elevations);
- (iii) with accurately measured metallicities (see §3.2) $12 + \log(\text{O}/\text{H}) > 8.5$ (where the CO -to- H_2 conversion is expected to be similar to, or lower than the Milky Way Value);
- (iv) lying in the redshift range, $0.01 < z < 0.03$
- (v) with an existing HI observation from the literature.

After applying these cuts to the parent SDSS spectroscopic catalogue, the final target list was determined based on the targets’ position on the sky, taking into account both the position of the Sun (targets too close to the Sun cannot be observed) and the position of potential flux calibrators.

The lower redshift bound of the final selection criterion has been chosen so as to ensure that the $\sim 27''$ APEX beam at 230 GHz covers the area of CO emission. Galaxies observed at lower redshifts have a high probability that their CO line emission will be larger than the size of the beam. As a final check, we manually checked the optical extent of all galaxies to ensure that they fall approximately within the APEX beam (the few galaxies which have slightly larger optical extents are still small enough to have most of their CO emitting regions within the beam – see §4.0.1 for discussion). The high-redshift cutoff has been chosen so as to keep the integration times reasonable given the expected faintness of low-J CO line emission in more distant objects (particularly considering the low stellar masses and metallicities of our sample).

We note that our selection criteria on the metallicity is sufficient to cover the expected range in metallicities for SDSS galaxies over our stellar mass range, $8.5 < \log(M_*) < 10.0$. As discussed above, lower metallicity galaxies typically have increased values of α_{CO} and therefore the detection of $\text{CO}(2-1)$ line emission becomes unfeasible for APEX. Our selection criteria leaves us with a sample of late-type galaxies which have a range of estimated star-formation rates ($0.01 < \log(\text{SFR}/M_{\odot} \text{ yr}^{-1}) < 2.5$), and metallicities ($8.5 < [12 + \log \text{O}/\text{H}] < 9.2$).

Table B1 lists the physical properties of the galaxies in the ALLSMOG sample.

3 ANCILLARY OBSERVATIONS

3.1 HI overlap

At the relatively low stellar masses probed by our survey, it is likely that galaxies will have substantial (or even dominant) contributions to their total gas content coming from HI (e.g. Bothwell et al. 2009; Lagos et al. 2011). In order to be able to measure the *total* gas content ($\text{H}_2 + \text{HI}$), as well as explore any trends in the H_2/HI ratio, we ensured that every member of the ALLSMOG sample had an archival HI observation, generally from either the HI Parkes All Sky Survey (HIPASS) (Meyer et al. 2004), The Arecibo Legacy Fast ALFA Survey (ALFALFA) (Haynes et al. 2011), or –

³ <http://www.mpa-garching.mpg.de/SDSS/DR7/>

failing either of these – from the large collection of H I observations assembled by Springob et al. (2005). Given our sample selection was from the SDSS spectroscopic survey, the majority of the ALLSMOG sample also appears in the ALFALFA survey.

3.2 Deriving physical parameters

Our sample galaxies are selected from the SDSS spectroscopic survey, and have their stellar masses and star formation rates readily available. We adopt both stellar masses and star formation rates (corrected for fibre aperture effects) as listed in the MPA-JHU catalogue.

We derive gas-phase metallicities using the available optical strong-line fluxes, and the calibration given in Maiolino et al. (2008), which uses a combination of models and empirical calibration. Specifically, we use two diagnostics, the $N[\text{II}]/\text{H}\alpha$ ratio and the ‘R23’ parameter ($= ([\text{OII}]3727 + [\text{OIII}]4958, 5007)/\text{H}\beta$), and derive a metallicity based on each. We take as our final metallicity measurement the mean of the two derivations: any galaxies for which the two methods produce metallicities which are discrepant by > 0.2 dex were discarded at the sample-selection phase, and do not appear in our final sample.

4 OBSERVATIONS AND DATA REDUCTION

Observations of the CO(2 – 1) line were carried out during 2013 and 2014 using the 230 GHz Swedish Heterodyne Facility Instrument (SHFI; Vassilev et al. 2008) on the APEX telescope, located at Llano Chajnantor in Chile. Observing conditions over the two semesters varied from relatively poor to excellent (precipitable water vapour $0.2 < (\text{PWV}/\text{mm}) < 3$), with typical average conditions of $\text{PWV} \sim 2$ mm. Focusing was determined using planets (Jupiter or Saturn) approximately every 2 hours. Pointing corrections were carried out once per hour using a bright quasar close to the science target.

Data were reduced using the CLASS package in GILDAS⁴. All observations were examined by hand, scan by scan, and any individual scans displaying significant distortions, like baseline ripples, were discarded. Typical final spectral noise levels (after removing bad scans) were ~ 2 mK per 20 km s^{-1} channel. For consistency and ease of use, we hereafter convert all flux and noise values from Kelvin to Janskys: the APEX-1 receiver has a telescope efficiency at 230 GHz of 39 Jy/K, estimated using the Ruze formula. Typical spectral noise levels therefore, in mJy, are ~ 80 mJy per 20 km s^{-1} channel. (Noise levels for individual observations are listed in Table B2.) We also calculate an aperture correction factor, to correct for potential CO flux falling outside the $27''$ beam – in the majority of cases, essentially all the CO flux falls within the beam (the mean amount of flux falling inside the beam is $92 \pm 7\%$). Appendix Section A gives more details of this correction factor. Individual correction factors are listed in Tab. B2, and all CO luminosities and H_2 masses hereafter are corrected for aperture effects.

Final reduced spectra were binned to 20 km s^{-1} resolution, and further analysed in IDL. CO(2 – 1) flux densities were measured by velocity-integrating Gaussian profiles fit to the central emission line. Gaussian profiles were chosen in order to simultaneously measure the line width, flux density, and any potential continuum contribution. All but two sources were well-fit by single Gaussian profiles: the two exceptions, 2MASJ0846+02 and NGC2936, had significant non-Gaussian emission and were poorly fit by a single profile. For these sources, we fit double Gaussian profiles (Figs B1 and B3). CO luminosities were then calculated using the standard relation given by Solomon & Vanden Bout (2005):

$$L'_{\text{CO}} = 3.25 \times 10^7 S_{\text{CO}} \Delta v \nu_{\text{obs}}^{-2} D_L^2 (1+z)^{-3}, \quad (1)$$

where L'_{CO} is the line luminosity in $\text{K km s}^{-1} \text{ pc}^2$, $S\Delta v$ is the velocity-integrated CO line flux in Jy km s^{-1} , ν_{obs} is the observed frequency of the line in GHz, and D_L is the distance in Mpc. For the purposes of this work, we assume that the CO(2 – 1) line is fully thermalised – that is, we assume $T_b(2-1)/T_b(1-0) = 1$ (where T_b is the equivalent Rayleigh-Jeans brightness temperature in excess of that of the cosmic microwave background). Making the assumption that the CO(2 – 1) line is slightly sub-thermalised would raise our final derived CO(1 – 0) line luminosities by approximately 10% (for a typical brightness temperature ratio).

For sources not detected in CO, we calculate 3-sigma upper limits on the CO flux density based on the measured rms channel noise:

$$S_{\text{CO}} < 3\sigma \sqrt{\Delta V_{\text{CO}} dv}, \quad (2)$$

where $\sigma(\text{Jy})$ is the channel noise given in Table B2, ΔV_{CO} is the mean linewidth of the detected sample ($= 130 \text{ km s}^{-1}$), and dv is the bin size in km s^{-1} ($= 20 \text{ km s}^{-1}$).

Of the 42 sources observed to date, we detect 25 in CO(2 – 1) emission – a detection rate of 60%. Figure 1 shows histograms of redshift and stellar mass for the ALLSMOG sample, with CO detections and non-detections separated. It can be seen that there is no apparent redshift bias in our detection rates (Figure 1, left panel): a Kolmogorov-Smirnov test of the redshifts of the detected and non-detected subsamples returns a P value of 0.59, suggesting that there is no statistical difference between the two.

There is, on the other hand, a strong *stellar mass* bias in the detection rate (Fig. 1, right panel). Galaxies at lower stellar masses become increasingly difficult to detect in CO emission, with the result that essentially all galaxies below $10^9 M_{\odot}$ are non-detections. The exception, NGC2936 (which has a stellar mass $\log(M_*) = 8.5 M_{\odot}$), is undergoing a major merger (see appendix Fig. A3), and is significantly elevated above the ‘main sequence’ of star formation. Full details of our observations are listed in Table B2.

4.1 Deriving H_2 masses

Molecular hydrogen masses can be calculated from the CO luminosity, L'_{CO} , by assuming a CO/ H_2 conversion factor (which we refer to as α_{CO}):

$$M(\text{H}_2) = \alpha_{\text{CO}} L'_{\text{CO}} \quad (3)$$

⁴ <http://www.iram.fr/IRAMFR/GILDAS/>

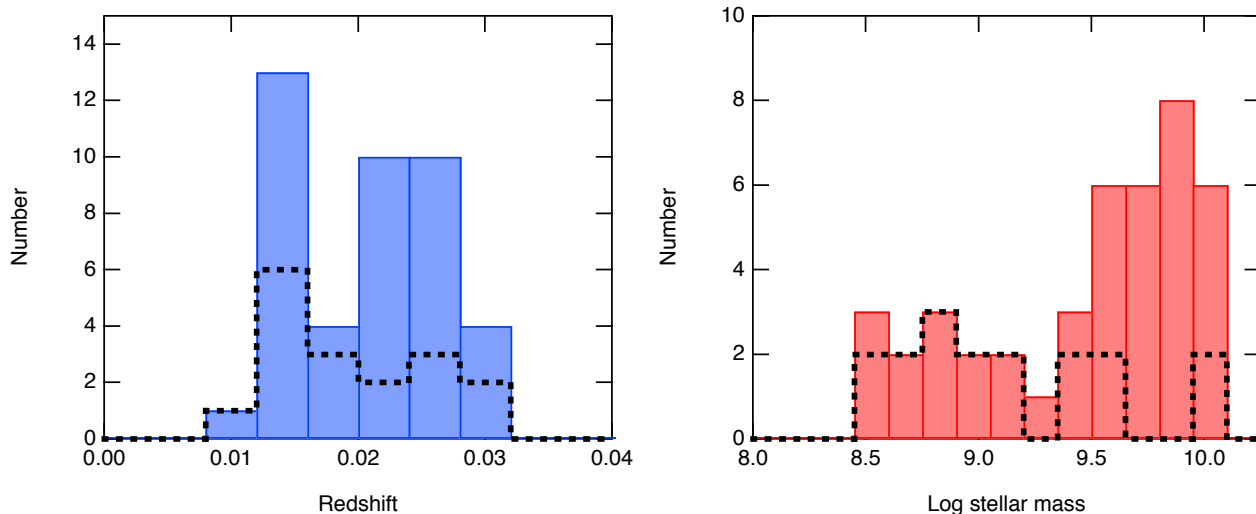


Figure 1. Histograms of the numbers of galaxies in the ALLSMOG sample, showing the distribution in distance (*Left Panel*) and stellar mass (*Right Panel*). In each, the full ALLSMOG sample is traced by a coloured histogram, while non-detections are traced by a dashed line. While the distribution in redshift is relatively independent of detection status, galaxies at lower stellar masses have a poorer detection rate than those at higher stellar masses.

As discussed above, while a number of physical factors can cause α_{CO} to vary, it is likely that one of the dominant factors is metallicity, with α_{CO} increasing as metallicity decreases. As such, throughout this work we will present results assuming two cases:

(i) A constant, Milky-Way appropriate conversion factor of $\alpha_{\text{CO}} = 4.5 \text{ M}_{\odot} (\text{K km s}^{-1} \text{ pc}^2)^{-1}$; (Bolatto et al. 2013). The units of α_{CO} are hereafter omitted. This value includes a correction of 1.36 to account for interstellar helium.

(ii) A conversion factor which is derived galaxy by galaxy, dependent on the gas-phase metallicity.

There are a number of metallicity-dependent CO/H₂ conversion factors in the literature (Bolatto et al. 2013 presents a compilation of several recent ones). In the interest of brevity, we will not present all plots for every available conversion factor. Instead, we will plot results assuming both a constant α_{CO} , and the metallicity-dependent conversion factor derived by Wolfire et al. (2010). The Wolfire et al. (2010) conversion factor models α_{CO} as relatively flat at high (\sim solar) metallicities, with a sharply non-linear increase towards higher values of α_{CO} as metallicity decreases. Bolatto et al. (2013) note that the Wolfire et al. (2010) α_{CO} prediction provides the best fit to existing data (Sandstrom et al. 2013).

In addition, we will also discuss the effect on our results of using some additional recent metallicity-dependent conversion factors: those presented by Israel (1997), Glover & Mac Low (2011), Feldmann et al. (2012), and Narayanan et al. (2012). Over the metallicity range occupied by our sample ($12 + \log(\text{O}/\text{H}) > 8.5$), most common metallicity-dependent conversion factors exhibit relatively small differences – the two ‘outlier’ conversion factor prescriptions, predicting the most extreme values of α_{CO} , are Narayanan et al. (2012) (which predicts the lowest values of α_{CO}), and Israel (1997) (which predicts the steepest metallicity dependence, and produces values of α_{CO} which trace the upper envelope

of measured values for galaxies with sub-solar metallicities). Fig. 9 in Bolatto et al. (2013) shows the relation between metallicity and α_{CO} for a range of conversion factors, including Wolfire et al. (2010). Any of our conclusions which are significantly altered by the use of one particular conversion factor will be highlighted below.

Table B3 lists derived gas masses, and other derived properties (including stellar masses, SFRs, and metallicities) for galaxies in ALLSMOG sample.

4.2 Comparison to other samples

Throughout this work, we compare the ALLSMOG sample to two other large surveys for molecular gas in the local Universe – COLDGASS and the Herschel Reference Survey (HRS). COLDGASS selects galaxies from the GASS survey with stellar masses $> 10^{10} \text{ M}_{\odot}$, while the HRS is a volume-limited sample of galaxies with distances $15 < D[\text{Mpc}] < 25$. Both samples have available optical spectra: COLDGASS galaxies are taken from the SDSS spectroscopic survey, and optical spectroscopy for the HRS was published by Boselli et al. (2013). For each of these samples, we also calculate metallicities identically as for ALLSMOG – the adopted metallicities are taken to be the mean of the two values calculated using the R23 parameter and the [NII]/H α ratio. As before, any galaxies exhibiting a discrepancy of > 0.2 dex between the two methods were deemed to have unreliable metallicity measurements, and were not used in this analysis.

We have calculated H₂ masses for these samples using the same method as for the ALLSMOG galaxies – by multiplying their observed CO luminosities by α_{CO} (both constant, and metallicity-dependent).

COLDGASS galaxies all appear in the SDSS spectroscopic survey, and – like ALLSMOG galaxies – have stellar masses and star formation rates available in the MPA-JHU catalogue. The HRS, however, contains very local galax-

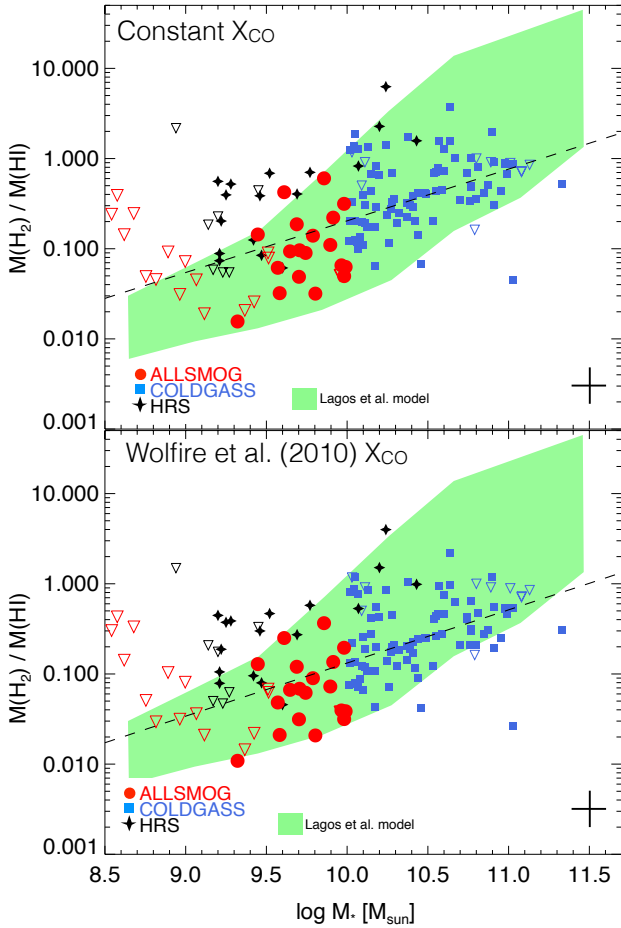


Figure 2. H_2/HI ratios, for the ALLSMOG sample. Also plotted are the galaxies from the COLDGASS and HRS surveys with well-defined metallicities (as described in the text). The panel has molecular gas masses calculated using a constant, Milky-Way α_{CO} . The lower panel has molecular gas masses calculated using the metallicity-dependent α_{CO} of Wolfire et al. (2010). Filled symbols and open triangles denote detected sources and 3σ upper limits, respectively. Black dotted lines show linear regression fits, estimated using a Bayesian MCMC technique to account for the upper limits. The green shaded region shows the semi-analytic model prediction from Lagos et al. (2011) (the upper and lower bounds of the coloured region mark the 90th and 10th percentiles of the model distribution).

ies which do not appear in the MPA-JHU catalogue. Stellar masses for the HRS galaxies are available in Cortese et al. (2012). We calculate star formation rates for the HRS galaxies using a combination of UV fluxes (from GALEX, published by Cortese et al. 2012) and IR fluxes (from the Spitzer Multi-Band Imaging Photometer (MIPS), published by Bendo et al. 2012). We calculate a FUV attenuation using the ‘IRX’ parameter, $IRX = \log(L_{IR}/L_{FUV,obs})$:

$$A(FUV) = -0.028X^3 + 0.392X^2 + 1.094X + 0.546, \quad (4)$$

where X is the IRX parameter (Burgarella et al. 2005). Star formation rates are then calculated from the extinction-corrected FUV luminosity, using

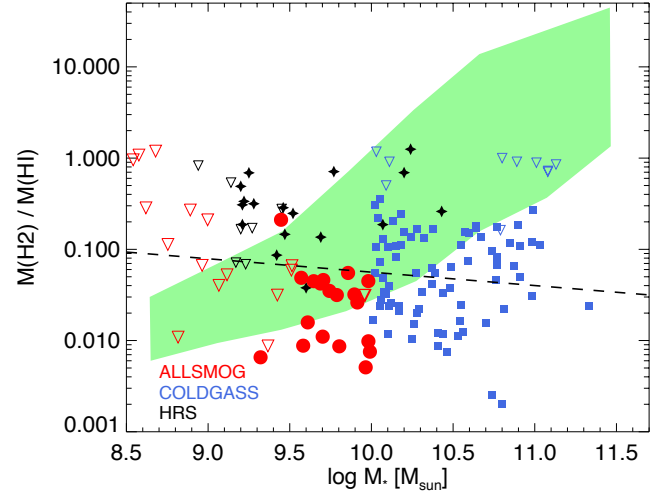


Figure 3. H_2/HI ratios, for the ALLSMOG sample, calculated using the Israel (1997) metallicity-dependent α_{CO} . Also plotted are the galaxies from the COLDGASS and HRS surveys with well-defined metallicities (as described in the text). Filled symbols and open triangles denote detected sources and 3σ upper limits, respectively. The black dotted line shows a linear regression fit, estimated using a Bayesian MCMC technique to account for the upper limits. The green shaded region shows the semi-analytic model prediction from Lagos et al. (2011) (the upper and lower bounds of the coloured region mark the 90th and 10th percentiles of the model distribution).

$$\log SFR = \log L_{FUV,corr} - 9.68, \quad (5)$$

which is a SFR prescription calculated specifically for the GALEX bands by Iglesias-Páramo et al. (2006), which we have modified by a factor of 1.5 to convert from their Salpeter (1955) IMF to the Kroupa (2001) IMF used to calculate SDSS parameters.

5 RESULTS AND DISCUSSION

5.1 The H_2/HI ratio

The ratio of molecular-to-atomic gas mass in galaxies is dependent on a range of physical processes, including the interstellar radiation field, the pressure of the ISM, and the abundance of dust (which aids the formation of molecules). The ALLSMOG survey, being a low-mass sample, is relatively HI rich compared to more massive samples (e.g., COLDGASS). When using a constant α_{CO} , we measure a mean H_2/HI ratio of 0.11, with a 1σ scatter of 0.42 dex. Using a metallicity-dependent α_{CO} , we measure a mean H_2/HI ratio of 0.08, with a 1σ scatter of 0.41 dex.

Fig. 2 shows the H_2/HI mass ratio, plotted against stellar mass for ALLSMOG galaxies, and our two comparison samples, COLDGASS and HRS. For our two main choices of α_{CO} we find that the H_2/HI ratio increases with stellar mass.

Here (and in our subsequent analyses below) we use regression analysis to fit linear slopes to the data. We employ the IDL code `LINMIX_ERR`, developed by Kelly (2007) for this purpose. `LINMIX_ERR` is a Bayesian linear regression

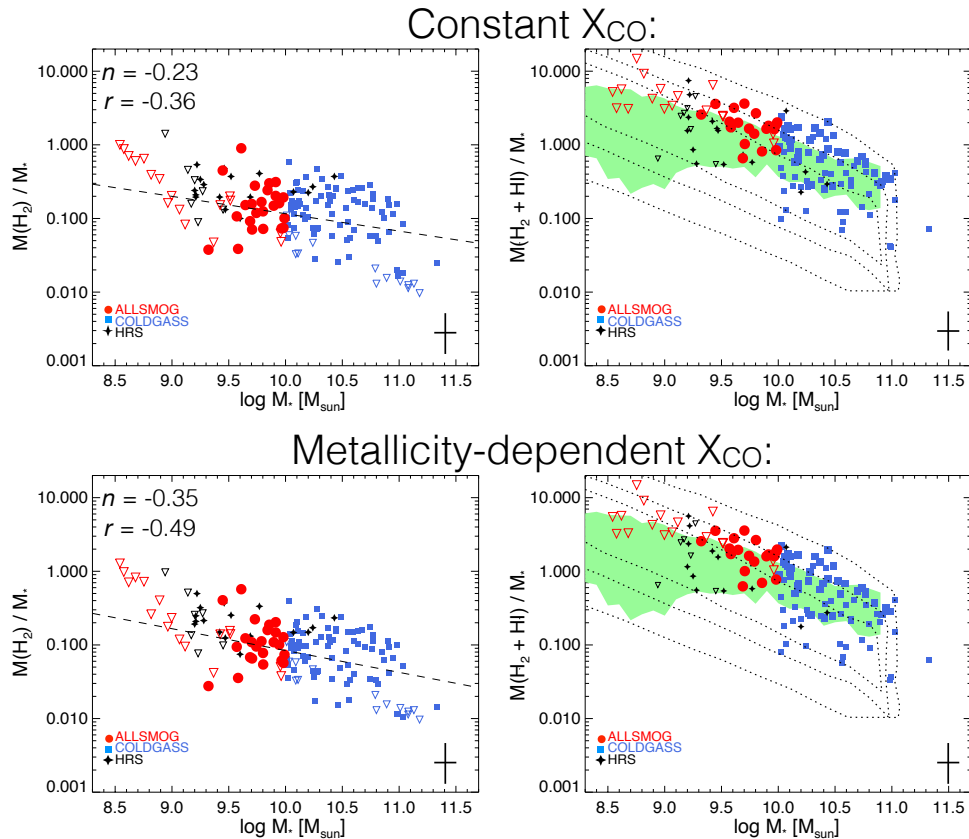


Figure 4. Gas fractions, plotted against stellar mass, for the ALLSMOG sample. Also plotted are the galaxies from the COLDGASS and HRS surveys with well-defined metallicities (as described in the text). Galaxies with upper limits on their gas mass are plotted with open triangles. The upper row of panels has molecular gas masses calculated using a constant, Milky-Way α_{CO} . The lower panels have molecular gas masses calculated using the metallicity-dependent α_{CO} of Wolfire. (2010). The left and right hand panels show (respectively), the molecular, and total gas fraction. Black dashed lines show linear regression fits to all three samples, estimated using a Bayesian MCMC technique to account for the upper limits. Inset legends give the slope of the fits n , and the Pearson correlation coefficients r . The green shaded area on the total gas fraction panels shows the predictions from cosmological hydrodynamical simulations (Davé et al. 2013), assuming momentum-conserving winds. Dotted contours on the total gas fraction panels mark 2σ , 4σ , 6σ contour levels for the distribution of galaxies in the analytic ‘gas regulator model’ predictions of Peng & Maiolino (2014).

estimator, which uses a Markov-Chain Monte Carlo method to fit datasets containing both upper limits, and detected datapoints with heteroscedastic errors.

Though there is considerable scatter at all stellar masses, simple linear regressions applied to the data suggest positive slopes, at high significance. Linear fits give a slope (n), for a constant α_{CO} , of $n = 0.66 \pm 0.08$, while the Wolfire et al. (2010) metallicity-dependent α_{CO} results in a slightly shallower slope of $n = 0.53 \pm 0.08$. Formal correlation coefficients (r) imply correlation strengths, for a constant α_{CO} , of $r = 0.66 \pm 0.06$ – using a Wolfire et al. (2010) metallicity-dependent factor weakens the correlation slightly, giving $r = 0.58 \pm 0.07$. All of the metallicity-dependent conversion factors produce an increase in the H_2/HI ratio, with the exception of the Israel (1997) factor, which produces a H_2/HI ratio which is flat (or even declining) with increasing stellar mass. This is shown in Fig. 3.

These linear fits are for illustrative purposes only, demonstrating that an increase in H_2/HI ratio with stellar mass exists for most choices of α_{CO} . It is unlikely that the true relation between H_2/HI ratio and $\log(M_*)$ is linear; semi-analytic models predict a non-linear increase in H_2/HI

ratio with $\log(M_*)$. We overplot on Fig. 2 (and Fig. 3) the predicted H_2/HI ratio from Lagos et al. (2011)⁵. Both a constant conversion factor, and a Wolfire et al. (2010) factor, produce a H_2/HI ratio distribution in very close accordance with the semi-analytic model data. In contrast, the approximately flat H_2/HI ratio distribution produced by a Israel (1997) α_{CO} is in conflict with these model predictions.

We note, though, that there are other semi-analytic models available: Lagos et al. (2011) also calculate H_2/HI ratios using a Bower et al. (2006) model (which invokes a different star formation quenching mechanism compared to the Baugh et al. (2005) model used above⁶), which slightly under-predicts the H_2/HI ratio relative to the data in our samples, though the increase in H_2/HI ratio with stellar mass – and therefore the tension with the Israel (1997) conversion factor – is preserved.

⁵ The data shown uses a Baugh et al. (2005) model.

⁶ Section 2.2 in Lagos et al (2011) explains the difference between the two models in more detail.

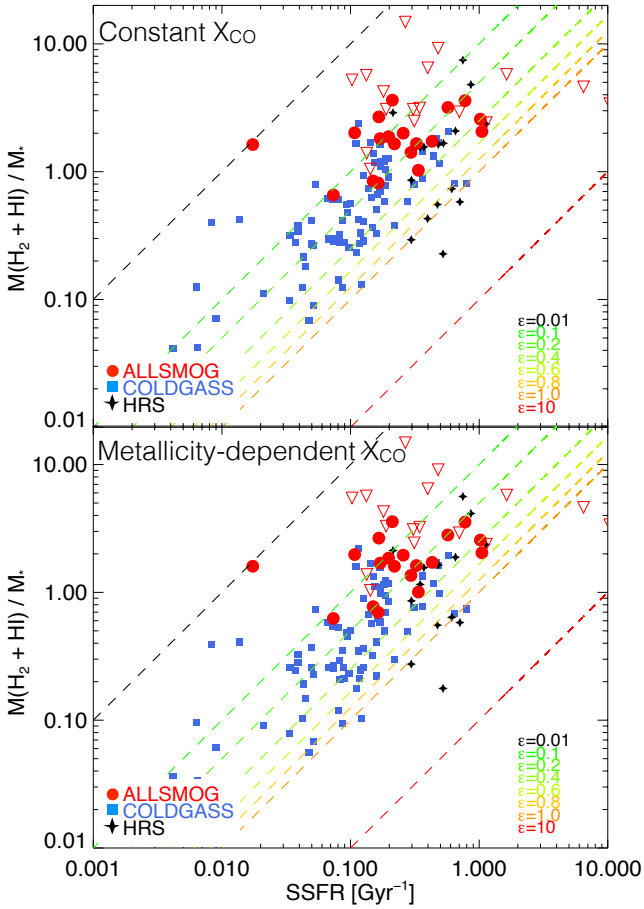


Figure 5. Gas fractions, plotted against specific star formation rate, for the ALLSMOG sample. Also plotted are the galaxies from the COLDGASS and HRS surveys with well-defined metallicities (as described in the text). The upper panel has molecular gas masses calculated using a constant, Milky-Way appropriate α_{CO} . The lower panel has molecular gas masses calculated using the metallicity-dependent α_{CO} of Wolfire et al. (2010). Dotted tracks show different star formation efficiencies (ϵ), ranging from 0.01 to 10 Gyr^{-1} (efficiencies greater than 1.0 are typically seen in starburst systems lying above the ‘main sequence’ of star formation). Star formation efficiencies are here defined in terms of the total (i.e., $\text{H I} + \text{H}_2$) gas content.

5.2 Gas fractions

Figure 4 shows gas fraction (defined here as M_{gas}/M_*) plotted against stellar mass for the ALLSMOG sample (as well as the COLDGASS and HRS comparison samples). The left and right hand panels respectively show the molecular and total gas fractions. In the upper set of panels, the molecular gas mass has been derived using a constant α_{CO} , while the lower set shows the molecular gas as derived using a metallicity-dependent α_{CO} .

In all cases, as expected, the molecular gas fraction decreases with increasing stellar mass. The molecular gas fraction decreases approximately monotonically with stellar mass (though with large scatter) across the entire mass range probed by the three samples, $10^9 \lesssim M_* \lesssim 10^{11}$.

As can be seen in Fig. 4, adopting the Wolfire et al. (2010) metallicity-dependent α_{CO} causes the gas fraction

vs. M_* relation to steepen, and become more tightly (anti-) correlated. Linear regressions applied to the molecular gas fraction data produce a slope of -0.23 ± 0.06 for a constant α_{CO} : when adopting the metallicity-dependent conversion factor, the slope steepens to -0.35 ± 0.05 . Likewise, the distributions are more tightly (anti-) correlated when using the metallicity-dependent α_{CO} . The Pearson correlation coefficient is $r = -0.36 \pm 0.09$ for a constant α_{CO} , while adopting the metallicity-dependent α_{CO} causes the correlation to tighten somewhat, to $r = -0.49 \pm 0.08$. These conclusions remain essentially identical if we use either of the four additional metallicity-dependent α_{CO} prescriptions given above: fitting to all galaxies using Feldmann et al. (2012) gives a slope of $n = -0.36 \pm 0.06$ and $r = -0.5$; a Glover & Mac Low (2011) factor gives $n = -0.26 \pm 0.04$ and $r = -0.39$, using Narayanan et al. (2012) gives $n = -0.45 \pm 0.04$ and $r = -0.61$, and using Israel (1997) gives by far the steepest value, $n = -0.86 \pm 0.07$ and $r = -0.70$. Across all our samples, we observe a monotonic decrease in molecular gas fraction with increasing stellar mass, which exists independent of the choice of CO/H_2 conversion factor.

The right hand panels of Fig. 4 show the *total* gas fraction, where ‘total gas’ is defined as $M(\text{H}_2) + M(\text{H I})$ (a 36% correction to account for helium is included in both of the CO/H_2 conversion factors) plotted against stellar mass. Due to the abundance of atomic gas in lower-mass systems (see §5.1 above), total gas fractions are, in general, far higher than the molecular fractions. We observe essentially the same trend, however: a monotonic decrease in total gas fraction across the entire stellar mass range of our samples. The mean total gas fraction for the ALLSMOG sample is 1.85.

It is difficult to quantify any trends in total gas fraction between the three samples, unfortunately, due to differing sample selection effects. While the ALLSMOG sample selected H I observations from publicly-available catalogs, the COLDGASS survey (as a subset of the GASS survey) was designed to observe deeper in H I than many other wide-field H I surveys. As a result, there is a clear selection effect-induced discontinuity in the distribution around $M_* = 10^{10} M_{\odot}$, with a subset of the more massive COLDGASS sample having far deeper H I data (and exhibiting lower total gas fractions) than ALLSMOG/HRS galaxies with $M_* < 10^{10} M_{\odot}$. As a result, we compare our gas fraction trends to simulations, but refrain from quantifying trends for the samples taken as a whole.

We have plotted on the right-hand panels of Fig. 4 gas fraction predictions from cosmological hydrodynamical simulations taken from Davé et al. (2013). We plot the model prediction which assumes ‘hybrid energy/momentum-driven winds’ winds (ezw in their nomenclature). We choose to compare our data to this ‘ezw’ model, as Davé et al. (2013) find this model matches observables (such as the H I mass function) better than their other wind models; for more details we refer readers to §2.1 of Davé et al. (2013).

In both the constant α_{CO} and metallicity-dependent α_{CO} cases, the Davé et al. (2013) hydrodynamical model predicts total gas fractions roughly in accordance with our data. Observed galaxies in our sample trace the ‘upper envelope’ of the model data, but this is to some extent to be expected (as our use of H I parent surveys provides samples of galaxies which are more H I rich than average).

As well as the hydrodynamic model predictions from

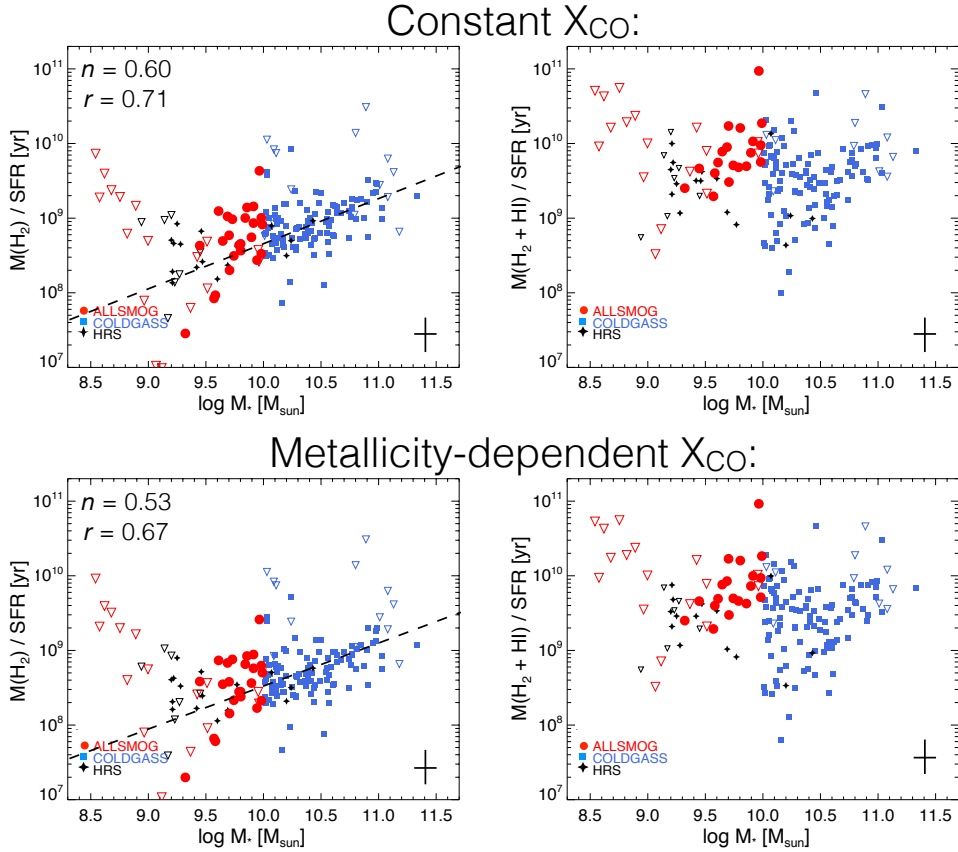


Figure 6. Gas consumption timescales, plotted against stellar mass, for the ALLSMOG sample. Also plotted are the galaxies from the COLDGASS and HRS surveys with well-defined metallicities (as described in the text). Filled symbols and open triangles denote detected sources and 3σ upper limits, respectively. The upper row of panels has molecular gas masses calculated using a constant, Milky-Way appropriate α_{CO} . The lower panels have molecular gas masses calculated using the metallicity-dependent α_{CO} of Wolfire et al. (2010). The left and right hand panels show (respectively), the molecular, and total gas fraction. There is a positive correlation between molecular gas consumption time and stellar mass, regardless of the choice of conversion factor. Linear regression fits to the molecular gas timescales are shown in the left panels: the slopes are 0.63 ± 0.06 for the constant α_{CO} , and 0.48 ± 0.06 for the metallicity-dependent α_{CO} . The inset caption gives the slope of the linear fit (n), and the Pearson correlation coefficient (r).

Davé et al. (2013), we also plot on Fig. 4 analytic predictions from the Peng & Maiolino (2014) ‘gas regulator’ model. This model (often called the ‘bathtub’ model) can predict galaxy behaviour by analytically solving coupled equations describing a small number of physical parameters – gas accretion, outflow, star formation and metal production. It can be seen in Fig. 4 that this analytical model produces a close match to the observed gas fraction data. While the majority of galaxies in all three surveys clearly represent gas-rich systems, the distribution, and in particular the monotonic slope of the gas fraction – stellar mass relation, is reproduced well by the Peng & Maiolino (2014) analytic model.

Figure 5 shows the total gas fraction as a function of the specific star formation rate ($\text{SSFR} = \text{SFR}/M_*$). Gas fraction correlates positively with specific star formation rate (with considerable scatter). This scatter can be interpreted in terms of star formation efficiency variations, whereby galaxies at a given gas fraction with higher star formation efficiencies have higher specific star formation rates (though the scatter in the H_2/HI ratio at a given stellar mass will contribute, due to the close dependence between SFR and H_2 content).

On Fig. 5 we have also shown ‘tracks’ of varying star formation efficiency, calculated using the expression:

$$f_g = \frac{\text{SSFR}}{\epsilon} \quad (6)$$

where f_g is the total gas-to-stellar mass ratio, and ϵ is the star formation efficiency, $\text{SFR}/M(\text{gas})$. This expression follows analytically from the definitions of SSFR and gas fraction.

It can be seen that the vast majority of the galaxies, across all three samples, lie within regions with implied star formation efficiencies of $0.1 < \epsilon/\text{Gyr}^{-1} < 1.0$. There are a few outliers with higher implied efficiencies, which are likely to be systems lying above the main sequence, undergoing a starburst event (caused by an interaction, or just stochastically clumpy gas accretion). Galaxies in the ALLSMOG sample have typical star formation efficiencies of $\epsilon < 0.5 (\text{Gyr})^{-1}$. No galaxies in the ALLSMOG sample – even those not detected in CO emission – imply star formation efficiencies $< 0.01 (\text{Gyr})^{-1}$.

5.3 Gas consumption timescales

It is also possible to interpret the ratio between gas mass and SFR in terms of a gas consumption timescale, defined here as $\tau_{\text{gas}} = M_{\text{gas}}/\text{SFR}$ ($= 1/\epsilon$).

Figure 6 shows the gas consumption timescales for the ALLSMOG sample (as well as the comparison samples, COLDGASS and the HRS). Fig. 6 is structured following Fig. 4 – the left and right hand panels show, respectively, the molecular and total gas consumption timescales, while the upper and lower panels calculate molecular gas masses using a constant α_{CO} (upper panels), and a Wolfire et al. (2010) metallicity-dependent α_{CO} (lower panels). The mean molecular gas consumption timescale for the ALLSMOG galaxies detected in CO is 0.78 ± 0.1 Gyr for a constant α_{CO} and 0.50 ± 0.1 Gyr for the metallicity-dependent α_{CO} . The rms scatter in $\log(\tau_{\text{H}_2})$ is 0.44 dex.

We confirm the trends found by both Saintonge et al. (2011) and Boselli et al. (2014): that the molecular gas consumption timescale τ_{H_2} is not constant, but increases with stellar mass over the full mass range of the detected samples ($M_* \gtrsim 10^9 M_{\odot}$). Molecular gas depletion timescales vary from ~ 2 Gyr at the most massive end of the distribution inhabited by COLDGASS galaxies ($M_* > 10^{11} M_{\odot}$), to ~ 100 Myr for the lowest mass detected galaxies ($M_* \sim 10^9 M_{\odot}$).

However, in addition to this finding (and in opposition to the results of Boselli et al. 2014), we find that this positive trend persists, even when using a non-constant CO/H₂ conversion factor. Again, applying the linear regression analysis discussed above, we find that when using a constant α_{CO} , τ_{H_2} increases with stellar mass with a slope of 0.60 ± 0.06 (and a Pearson correlation coefficient of $r = 0.71$). Employing the Wolfire et al. (2010) metallicity-dependent α_{CO} flattens the relation slightly, but the correlation still persists, with a slope of 0.53 ± 0.07 (and $r = 0.67$). Indeed, we find this positive correlation between gas consumption timescale and stellar mass persists at high significance when using three of the four additional metallicity-dependent α_{CO} prescriptions listed in §4.1 above: a Feldmann et al. (2012) conversion factor results in a slope of index 0.46 ± 0.07 ($r = 0.61$); using Glover & Mac Low (2011) produces a slope of index 0.59 ± 0.06 ($r = 0.70$); and Narayanan et al. (2012) produces a slope of 0.41 ± 0.07 ($r = 0.56$).

In contrast to these findings, use of the Israel (1997) conversion factor produces an essentially flat relationship between molecular gas consumption timescale and stellar mass (albeit with nearly an order of magnitude scatter), with a slope of -0.11 ± 0.10 (and $r = -0.13$). This (close to) flat relationship would imply an approximately constant molecular gas consumption timescale of $\log \tau_{\text{H}_2} = 8.25 \pm 0.71$ yr across all three samples.

While the use of a constant, Milky-Way value for α_{CO} produces the strongest (and steepest) positive correlation between gas consumption timescale and stellar mass, the correlation, whereby the most massive galaxies have molecular gas consumption timescales over an order of magnitude longer than the least massive galaxies observed here, persists for three of the four metallicity-dependent CO/H₂ conversion factors used in this work. As above with the H₂/HI ratio, the exception to this is the Israel (1997) conversion factor, which produces a relation between H₂ consumption time and stellar mass which is approximately flat.

The relation between *total* gas consumption time and stellar mass is more difficult to interpret from the samples used in this work, due to the HI selection effects mentioned above. Certainly, at stellar masses $< 10^{10} M_{\odot}$ the detected ALLSMOG galaxies show signs of a positive correlation between τ_{gas} and M_* . Due to the differing HI sample selection effects above and below $10^{10} M_{\odot}$, however, it is difficult to identify any trends existing across the full mass range. It is likely that deep dedicated HI observations at low stellar masses are required in order to fully examine trends in total gas consumption timescale.

6 SUMMARY

We have presented the initial data release and analysis from the ALLSMOG survey, a public legacy survey for molecular gas in local low-mass galaxies. We have used APEX to observe the CO(2–1) emission line in 42 galaxies with stellar masses in the range $8.5 < \log(M_*/M_{\odot}) < 10$, redshifts in the range $0.01 < z < 0.03$, and metallicities $12 + \log(\text{O}/\text{H}) > 8.5$. We detect a total of 25 of 42 galaxies observed – a detection rate of 60%. There is a strong stellar mass bias in the detection statistics, with all galaxies with stellar masses $M_* < 10^9 M_{\odot}$ (with one exception) being undetected.

We use our metallicities, derived using optical strong line methods, to calculate metallicity-based CO/H₂ conversion factors, avoiding the unphysical assumption of a constant α_{CO} . Our main conclusions are as follows:

(i) The ratio $M(\text{H}_2)/M(\text{HI})$ increases with stellar mass, albeit with large scatter, in agreement with both semi-analytic predictions and previous work. Importantly, this result remains robust when using a constant CO/H₂ conversion factor, and three of the four metallicity-dependent CO/H₂ conversion factors used in this work. The exception – the Israel (1997) α_{CO} – produces a $M(\text{H}_2)/M(\text{HI})$ ratio which is roughly flat with stellar mass, in conflict with model predictions.

(ii) Molecular gas fractions decrease with increasing stellar mass – this conclusion holds independent of the choice of CO/H₂ conversion factor. Total gas fractions (H₂+HI+He) also decrease with stellar mass, in accordance with predictions from both analytic and hydrodynamical models

(iii) We confirm the non-universality of the molecular gas consumption timescale across 2 orders of magnitude in stellar mass, finding depletion timescales varying monotonically from ~ 2 Gyr at the massive end of the distribution (inhabited by COLDGASS galaxies) to ~ 100 Myr for the lowest mass galaxies in our survey. Again, we find that this result persists when using a constant conversion factor, and three of the four CO/H₂ conversion factor prescriptions used in this work. Use of the Israel (1997) conversion factor produces a molecular gas consumption time which is approximately constant.

ACKNOWLEDGMENTS

This publication is based on data acquired with the Atacama Pathfinder Experiment (APEX), with ESO programme ID number 192.A-0359. APEX is a collaboration between the Max-Planck-Institut für Radioastronomie, the European Southern Observatory, and the Onsala Space Observatory. We would like to extend our thanks to the staff of the APEX observatory for their support while observing these data, and to the anonymous referee whose comments helped improve this manuscript. This research has made use of NASA's Astrophysics Data System. This work was co-funded under the Marie Curie Actions of the European Commission (FP7-COFUND).

REFERENCES

- Baugh C. M., Lacey C. G., Frenk C. S., Granato G. L., Silva L., Bressan A., Benson A. J., Cole S., 2005, *M.N.R.A.S.*, 356, 1191
- Bendo G. J., Galliano F., Madden S. C., 2012, *M.N.R.A.S.*, 423, 197
- Bolatto A. D., Wolfire M., Leroy A. K., 2013, *ARAA*, 51, 207
- Boselli A., Cortese L., Boquien M., 2014, *ArXiv e-prints*
- Boselli A., Cortese L., Boquien M., Boissier S., Catinella B., Lagos C., Saintonge A., 2014, *ArXiv e-prints*
- Boselli A., Eales S., Cortese L., Bendo G., Chaniel P., Buat V., Davies J., Auld R., et al., 2010, *P.A.S.P.*, 122, 261
- Boselli A., Hughes T. M., Cortese L., Gavazzi G., Buat V., 2013, *Astron. Astrophys.*, 550, A114
- Bothwell M. S., Chapman S. C., Tacconi L., Smail I., Ivison R. J., Casey C. M., et al., 2010, *M.N.R.A.S.*, 405, 219
- Bothwell M. S., Kennicutt R. C., Lee J. C., 2009, *M.N.R.A.S.*, 400, 154
- Bothwell M. S., Smail I., Chapman S. C., Genzel R., Ivison R. J., Tacconi L. J., Alaghband-Zadeh S., Bertoldi F., Blain A. W., Casey C. M., Cox P., Greve T. R., Lutz D., Neri R., Omont A., Swinbank A. M., 2013, *M.N.R.A.S.*, 429, 3047
- Bower R. G., Benson A. J., Malbon R., Helly J. C., Frenk C. S., Baugh C. M., Cole S., Lacey C. G., 2006, *M.N.R.A.S.*, 370, 645
- Brinchmann J., Charlot S., White S. D. M., Tremonti C., Kauffmann G., Heckman T., Brinkmann J., 2004, *M.N.R.A.S.*, 351, 1151
- Burgarella D., Buat V., Iglesias-Páramo J., 2005, *M.N.R.A.S.*, 360, 1413
- Carilli C. L., Walter F., 2013, *ARAA*, 51, 105
- Catinella B., Schiminovich D., Kauffmann G., Fabello S., Wang J., Hummels C., Lemonias J., Moran S. M., et al., 2010, *M.N.R.A.S.*, 403, 683
- Cortese L., Boissier S., Boselli A., Bendo G. J., Buat V., Davies J. I., Eales S., Heinis S., Isaak K. G., Madden S. C., 2012, *Astron. Astrophys.*, 544, A101
- Davé R., Katz N., Oppenheimer B. D., Kollmeier J. A., Weinberg D. H., 2013, *M.N.R.A.S.*, 434, 2645
- Feldmann R., Gnedin N. Y., Kravtsov A. V., 2012, *ApJ*, 747, 124
- Genzel R., Tacconi L. J., Combes F., Bolatto A., Neri R., Sternberg A., et al., 2011, *ArXiv e-prints*
- Glover S. C. O., Mac Low M.-M., 2011, *M.N.R.A.S.*, 412, 337
- Greve T. R., Bertoldi F., Smail I., Neri R., Chapman S. C., Blain A. W., Ivison R. J., Genzel R., Omont A., Cox P., Tacconi L., Kneib J., 2005, *M.N.R.A.S.*, 359, 1165
- Haynes M. P., Giovanelli R., Martin A. M., Hess K. M., Saintonge A., Adams E. A. K., Hallenbeck G., Hoffman G. L., et al., 2011, *AJ*, 142, 170
- Iglesias-Páramo J., Buat V., Takeuchi T. T., Xu K., Boissier S., Boselli A., Burgarella D., Madore B. F., Gil de Paz A., et al., 2006, *ApJS*, 164, 38
- Israel F. P., 1997, *Astron. Astrophys.*, 328, 471
- Ivison R. J., Papadopoulos P. P., Smail I., Greve T. R., Thomson A. P., Xilouris E. M., Chapman S. C., 2011, *M.N.R.A.S.*, 412, 1913
- Kauffmann G., Heckman T. M., White S. D. M., Charlot S., Tremonti C., Peng E. W., Seibert M., Brinkmann J., Nichol R. C., SubbaRao M., York D., 2003, *M.N.R.A.S.*, 341, 54
- Kelly B. C., 2007, *ApJ*, 665, 1489
- Keres D., Yun M. S., Young J. S., 2003, *ApJ*, 582, 659
- Kroupa P., 2001, *M.N.R.A.S.*, 322, 231
- Lagos C. D. P., Baugh C. M., Lacey C. G., Benson A. J., Kim H.-S., Power C., 2011, *M.N.R.A.S.*, 418, 1649
- Leroy A., Bolatto A. D., Simon J. D., Blitz L., 2005, *ApJ*, 625, 763
- Leroy A. K., Walter F., Bigiel F., Usero A., Weiss A., Brinks E., de Blok W. J. G., Kennicutt R. C., Schuster K.-F., Kramer C., Wiesemeyer H. W., Roussel H., 2009, *AJ*, 137, 4670
- Maiolino R., Nagao T., Grazian A., Cocchia F., Marconi A., Mannucci F., Cimatti A., Pipino A., et al., 2008, *Astron. Astrophys.*, 488, 463
- Meyer M. J., Zwaan M. A., Webster R. L., Staveley-Smith L., Ryan-Weber E., Drinkwater M. J., Barnes D. G., Howlett M., et al., 2004, *M.N.R.A.S.*, 350, 1195
- Narayanan D., Krumholz M. R., Ostriker E. C., Hernquist L., 2012, *M.N.R.A.S.*, 421, 3127
- Peng Y., Maiolino R., 2014, *ArXiv e-prints*
- Riechers D. A., Carilli L. C., Walter F., Weiss A., Wagg J., Bertoldi F., Downes D., Henkel C., Hodge J., 2011, *ApJL*, 733, L11
- Saintonge A., Kauffmann G., Kramer C., Tacconi L. J., Buchbender C., Catinella B., Fabello S., Graciá-Carpio J., et al., 2011, *M.N.R.A.S.*, 415, 32
- Saintonge A., Kauffmann G., Wang J., Kramer C., Tacconi L. J., Buchbender C., Catinella B., Graciá-Carpio J., et al., 2011, *M.N.R.A.S.*, 415, 61
- Salpeter E. E., 1955, *ApJ*, 121, 161
- Sandstrom K. M., Leroy A. K., Walter F., Bolatto A. D., Croxall K. V., Draine B. T., Wilson C. D., Wolfire M., et al., 2013, *ApJ*, 777, 5
- Santini P., Maiolino R., Magnelli B., Lutz D., Lamastra A., Li Causi G., Eales S., Andreani P., et al., 2014, *Astron. Astrophys.*, 562, A30
- Schruba A., Leroy A. K., Walter F., Bigiel F., Brinks E., de Blok W. J. G., Dumas G., Kramer C., Rosolowsky E., Sandstrom K., Schuster K., Usero A., Weiss A., Wiesemeyer H., 2011, *AJ*, 142, 37
- Scoville N., Aussel H., Sheth K., Scott K. S., Sanders D., Ivison R., Pope A., Capak P., Vanden Bout P., Manohar S., Kartaltepe J., Robertson B., Lilly S., 2014, *ApJ*, 783,

84

- Solomon P. M., Vanden Bout P. A., 2005, *ARAA*, 43, 677
 Springob C. M., Haynes M. P., Giovanelli R., Kent B. R., 2005, *ApJS*, 160, 149
 Tacconi L. J., Neri R., Chapman S. C., Genzel R., Smail I., Ivison R. J., Bertoldi F., Blain A., Cox P., Greve T., Omont A., 2006, *ApJ*, 640, 228
 Tacconi L. J., Neri R., Genzel R., Combes F., Bolatto A., Cooper M. C., Wuyts S., Bournaud F., et al., 2013, *ApJ*, 768, 74
 Tremonti C. A., Heckman T. M., Kauffmann G., Brinchmann J., Charlot S., White S. D. M., Seibert M., Peng E. W., Schlegel D. J., Uomoto A., Fukugita M., Brinkmann J., 2004, *ApJ*, 613, 898
 Vassilev V., Meledin D., Lapkin I., Belitsky V., Nyström O., Henke D., Pavolotsky A., Monje R., et al., 2008, *Astron. Astrophys.*, 490, 1157
 Weiß A., De Breuck C., Marrone D. P., Vieira J. D., Aguirre J. E., Aird K. A., Aravena M., Ashby M. L. N., et al., 2013, *ApJ*, 767, 88
 Wolfire M. G., Hollenbach D., McKee C. F., 2010, *ApJ*, 716, 1191
 Young J. S., Xie S., Tacconi L., Knezek P., Viscuso P., Tacconi-Garman L., Scoville N., Schneider S., Schloerb F. P., Lord S., Lesser A., Kenney J., Huang Y.-L., Devoreux N., Claussen M., Case J., Carpenter J., Berry M., Allen L., 1995, *ApJS*, 98, 219

APPENDIX A: APERTURE CORRECTION CALCULATIONS

In order to derive total gas masses it is necessary to derive aperture correction factors, to correct for any potential flux lying outside the beam emitting area.

To account for this possible source of uncertainty, we calculate for each ALLSMOG galaxy a ‘beam coverage correction’, which will allow us to correct for potential missing flux due to the beam being smaller than the CO emitting region. B-band sizes (in terms of r_{25} , the 25th magnitude isophote) are available for each ALLSMOG galaxy, and are listed in Table B1. We calculate predicted CO exponential disc scaling lengths, h , using the relation derived from resolved CO observations (Young et al. 1995; Leroy et al. 2009), $h_{CO(2-1)} = 0.2 \pm 0.05r_{25}$.

An exponential disc has a radial surface brightness profile given by

$$I(R) = I(0)e^{(-R/h)}, \quad (\text{A1})$$

where $I(0)$ is the central brightness (irrelevant here, as we are simply interested in the percentage of the total flux recovered by the beam), R is the radius, and h is the scaling length.

For each galaxy, we integrate its exponential disc model out to the radius covered by the 27'' beam. However, inclination effects must also be taken into account. For a fully face-on galaxy, the fraction of flux falling within the beam will be given by integrating a 2D exponential disc model out to the beam radius (relative to the total flux):

$$\text{Flux fraction} = \frac{\int_0^{2\pi} \int_0^{\text{Beam}} e^{-R/h} R dr d\theta}{\int_0^{2\pi} \int_0^{\infty} e^{-R/h} R dr d\theta} \quad (\text{A2})$$

At higher inclination angles, more CO flux will fall inside the beam, and the solution will tend towards a 1D exponential model (for a fully edge-on galaxy):

$$\text{Flux fraction} = \frac{\int_0^{\text{Beam}} e^{-R/h} dR}{\int_0^{\infty} e^{-R/h} dR} \quad (\text{A3})$$

We therefore calculate a flux correction for each ALLSMOG galaxy by taking a linear combination of these two extreme situations, with the relative contribution from each given by the inclination angle i :

$$F = (\sin i) \left(\frac{\int_0^{\text{Beam}} e^{-R/h} dR}{\int_0^{\infty} e^{-R/h} dR} \right) + (1 - \sin i) \left(\frac{\int_0^{2\pi} \int_0^{\text{Beam}} e^{-R/h} R dR d\theta}{\int_0^{2\pi} \int_0^{\infty} e^{-R/h} R dR d\theta} \right) \quad (\text{A4})$$

It can be seen that at $i = 0^\circ$ and $i = 90^\circ$, this expression becomes the face-on and edge-on solutions (respectively).

We have empirically tested this technique using resolved CO(2 – 1) maps of the HERACLES sample (Leroy et al. 2009). We manually redshifted each HERACLES CO(2 – 1) map, so that their optical diameters spanned a range $25 < D_{25}'' < 100$ (approximately the range of diameters in the ALLSMOG sample). For each HERACLES galaxy, we then calculated how much of the total CO(2 – 1) flux would be recovered by a 27'' beam as a function of its size. The results are shown in Fig. A1 (left). There is a clear inclination effect (at a given optical size, a face-on galaxy will have more of its flux outside the beam than an edge-on galaxy). We have also plotted on Fig. A1 (left) the analytic solutions found by integrating 1D and 2D exponential functions (Equations A2 and A3). As expected, the two cases define the approximate boundaries to the distribution, with the 2D solution being a good model for the most face-on galaxies, and the 1D solution being a good model for the most edge-on galaxies.

The right panel of Fig. A1 shows the flux fraction for various inclinations, as predicted by Eq. A4. There is a good match between the model and the HERACLES data, and as such we adopt this method for calculating aperture corrections for the ALLSMOG sample. In the four cases where no inclination angle is listed for an ALLSMOG galaxy, we adopt an inclination-averaged angle of $\langle \sin i \rangle = \pi/4$ ($\theta \sim 51.7^\circ$ – see appendix A of ? for the derivation of this value).

Table B2 lists the percentage of the total flux recovered by our observations, calculated using Eq. A4. All CO luminosities and H₂ gas masses used throughout this work (and listed in Table AB) are calculated with this beam coverage correction applied.

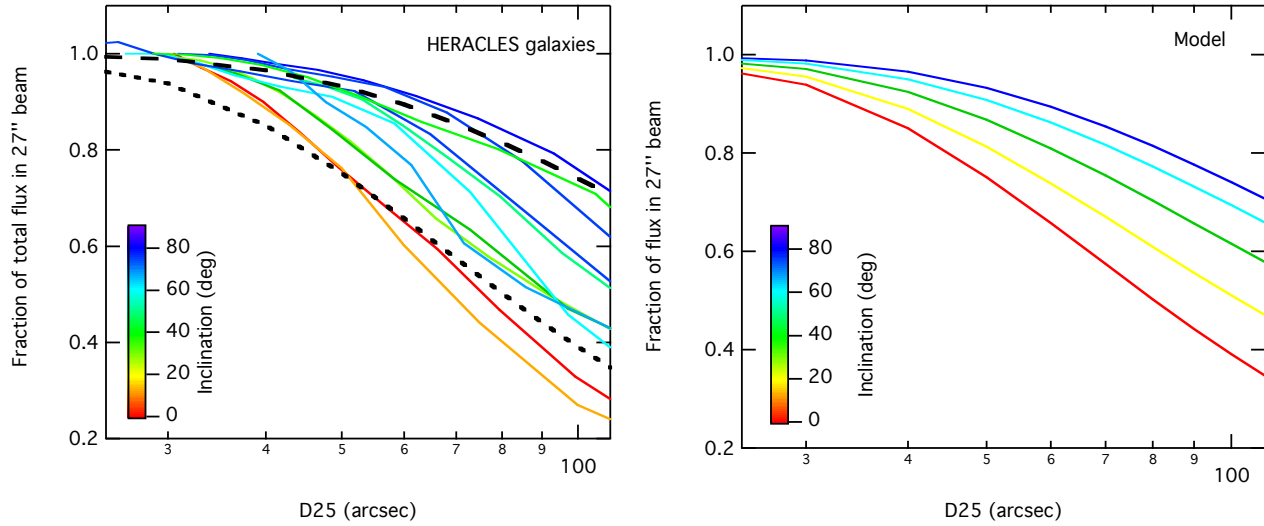


Figure A1. Plots showing the fraction of total CO(2 – 1) flux is recovered by a 27'' beam, plotted against the optical size of the galaxy. The left panel shows empirically measured flux fractions, taken from maps of the HERACLES sample (Leroy et al. 2011) where we have manually redshifted each map to simulate a range of sizes. The coloured lines show individual galaxies, while the black dotted and dashed lines show the 2D and 1D exponential solutions, respectively. While it is clear that the flux fraction drops as a function of optical size, there is also an inclination effect (by which at a given optical size, a face-on galaxy will have more of its flux outside the beam than an edge-on galaxy). As expected, 1D and 2D analytical solutions effectively define the boundaries of the distribution, being good matches for the most edge on and face on galaxies, respectively. The right panel shows the predicted flux fractions, calculated using model given in Eq. A4.

APPENDIX B: DATA TABLES

Table B1. Physical properties of the ALLSMOG sample. Column (1): Source name from NED. Columns (2) and (3): RA and DEC of SDSS source. Column (4): SDSS spectral redshift. Column (5): Morphological type from NED (blank if unavailable). Column (6): Log of the B-band optical diameter, in units of 0.1 arcmin.

(1) Full name	(2) RA [J2000]	(3) DEC [J2000]	(4) Redshift [z]	(5) Morphological Type [NED]	(6) Size log(0.1)d
UGC00272	00 27 49.7	-01 11 60	0.0130	Scd	1.128
IC0159	01 46 25.0	-08 38 12	0.0130	Scd	1.131
KUG0200-101	02 03 16.6	-09 53 26	0.0129	Sbc	0.810
UGC2004	02 31 59.6	+00 54 36	0.0218	SAB(s)c	0.850
UGC2529	03 05 29.6	-00 22 54	0.0248	S	0.928
NGC1234	03 09 39.1	-07 50 46	0.0124	Scd	1.198
SDSSJ0805+06	08 05 37.7	+06 59 35	0.0152	—	0.557
2MASXJ08393919+0349424	08 39 39.2	+03 49 43	0.0266	S0/a	0.642
2MASJ0846+02	08 46 54.0	+02 30 05	0.0282	Sa	0.588
2MASXJ08555592+0345300	08 55 56.0	+03 45 30	0.0275	—	0.729
2MASXJ08580528+0345228	08 58 05.3	+03 45 23	0.0269	S0/a	0.578
2MASXJ09105875+0752191	09 10 58.8	+07 52 19	0.0284	Sbc	0.754
UGC4977	09 21 59.6	+03 22 43	0.0278	Sc	0.924
MCG+00-25-005	09 36 35.4	+01 07 00	0.0164	Sb	0.855
SDSSJ0937+09	09 37 09.0	+09 27 51	0.0224	—	0.848
NGC2936	09 37 45.0	+02 45 34	0.0240	Irr	0.021
2MASXJ09393527+0624513	09 39 35.3	+06 24 52	0.0249	Scd	0.625
SDSSJ0950+11	09 50 11.2	+11 18 30	0.0188	—	0.465
2MASXJ10110944+0746489	10 11 09.4	+07 46 49	0.0262	Sc	0.843
2MASXJ10145891+0748028	10 14 58.9	+07 48 03	0.0283	Scd	0.743
IC0605	10 22 24.1	+01 11 54	0.0215	Sc	0.887
UGC5648	10 26 08.8	+04 22 22	0.0228	S	1.073
LEDA31382	10 35 42.3	+05 36 58	0.0272	Scd	0.871
NGC3436	10 52 28.9	+07 54 15	0.0205	Sab	0.935
SDSSJ1104+05	11 04 14.6	+05 07 37	0.0176	—	0.386
2MASXJ11103746+0411286	11 10 37.4	+04 11 29	0.0289	Sm	0.617
SDSSJ1112+09	11 12 50.2	+09 31 39	0.0209	—	0.768
MCG+00-29-013	11 18 49.6	+00 37 10	0.0254	Sc	0.761
UGC6329	11 18 56.2	+00 10 34	0.0249	Scd	0.905
UGC06838	11 51 56.1	-02 38 33	0.0129	SAab	0.850
IC3069	12 16 19.9	+10 09 39	0.0195	—	0.703
SDSSJ1328-02	13 28 46.9	-02 02 28	0.0124	—	0.750
MCG00-34-038	13 29 50.4	-01 25 45	0.0213	Sbc	0.826
CGCG017	13 32 50.2	-03 04 58	0.0142	Sbc	1.159
UGC085276	13 32 55.1	-01 09 34	0.0127	S?	0.933
NGC5405	14 01 09.5	+07 42 08	0.0230	S?	0.917
NGC5414	14 02 03.5	+09 55 46	0.0141	S?	0.988
UGC09359	14 33 15.8	-01 08 24	0.0138	Sdm	0.926
CGCG050-042	15 36 46.6	+07 50 01	0.0111	—	0.645
UGC10005	15 45 14.4	+00 46 20	0.0128	Sc	0.892
UGC11631	20 47 59.9	-00 10 48	0.0141	Scd	0.998
2MASXJ22350698-0845550	22 35 07.0	-08 45 55	0.0238	—	0.758

Table B2. Details of the APEX observations. Column (1): Source name from NED. Columns (2) and (3): RA and DEC of SDSS source. Column (4): spectral rms (per 20 km/s channel). Column (5): Total time on-source, after discarding distorted scans. Column (6): Flux density, and associated error, of the $^{12}\text{CO}(2-1)$ line. For non-detected galaxies, 3σ upper limits are quoted. Column (7): FWHM of the $\text{CO}(2-1)$ line, obtained by fitting a Gaussian profile. (8): Percentage of the CO flux recovered by the beam (see Appendix A)

(1) Name	(2) RA [J2000]	(3) DEC [J2000]	(4) rms ₍₂₀₎ [mJy]	(5) Time on source [Hours]	(6) S _{CO(2-1)} [Jy km/s]	(7) FWHM [km/s]	(8) Beam coverage [Fraction]
<i>Detected sources:</i>							
IC0159	01 46 25.0	-08 38 12	69	1.2	31.1 ± 5.8	157	0.77 ± 0.07
UGC2004	02 31 59.6	+00 54 36	131	0.8	114.9 ± 12.5	212	0.93 ± 0.03
NGC1234	03 09 39.1	-07 50 46	45	2.9	14.0 ± 3.5	132	0.71 ± 0.08
2MASJ0839+03	08 39 39.2	+03 49 43	96	0.6	30.0 ± 7.0	18	0.99 ± 0.01
2MASJ0846+02	08 46 54.0	+02 30 05	103	0.7	31.9 ± 5.4	36	0.99 ± 0.01
2MASJ0855+03	08 55 56.0	+03 45 30	41	0.8	29.7 ± 17.6	120	0.98 ± 0.02
2MASJ0858+03	08 58 05.3	+03 45 23	45	1.4	16.5 ± 5.9	41	0.99 ± 0.01
2MASJ0910+07	09 10 58.8	+07 52 19	90	0.5	40.3 ± 8.3	188	0.97 ± 0.02
UGC4977	09 21 59.6	+03 22 43	52	1.6	32.2 ± 5.2	216	0.92 ± 0.04
MCG00-25-005	09 36 35.4	+01 07 00	110	0.4	43.6 ± 8.7	139	0.93 ± 0.03
NGC2936	09 37 45.0	+02 45 34	160	0.3	416.4 ± 10.8	164	1.00 ± 0.00
2MASJ0939+06	09 39 35.3	+06 24 52	53	1.2	30.4 ± 5.6	247	0.99 ± 0.01
IC0605	10 22 24.1	+01 11 54	76	1.0	37.5 ± 6.8	174	0.90 ± 0.04
UGC5648	10 26 08.8	+04 22 22	69	0.9	28.4 ± 6.5	195	0.84 ± 0.07
NGC3436	10 52 28.9	+07 54 15	78	0.5	23.8 ± 5.2	98	0.88 ± 0.05
MCG00-29-013	11 18 49.6	+00 37 10	82	0.9	43.1 ± 7.6	188	0.94 ± 0.03
UGC6329	11 18 56.2	+00 10 34	47	1.6	11.1 ± 3.0	91	0.87 ± 0.05
UGC06838	11 51 56.1	-02 38 33	58	1.5	7.8 ± 3.0	51	0.95 ± 0.03
MCG00-34-038	13 29 50.4	-01 25 45	156	0.3	84.5 ± 8.5	84	0.94 ± 0.03
CGCG017	13 32 50.2	-03 04 58	100	0.8	49.3 ± 9.7	90	0.72 ± 0.07
UGC085276	13 32 55.1	-01 09 34	101	0.8	41.1 ± 7.0	58	0.87 ± 0.04
NGC5405	14 01 09.5	+07 42 08	109	0.5	20.2 ± 4.6	37	0.83 ± 0.07
NGC5414	14 02 03.5	+09 55 46	83	0.8	49.3 ± 9.3	91	0.86 ± 0.05
UGC11631	20 47 59.9	-00 10 48	35	4.4	29.5 ± 2.9	157	0.89 ± 0.05
2MASJ2235-08	22 35 07.0	-08 45 55	49	3.0	27.1 ± 3.4	106	0.96 ± 0.02
<i>Non-detected sources:</i>							
UGC00272	00 27 49.7	-01 11 60	63	0.9	< 9.6	—	0.79 ± 0.07
KUG0200	02 03 16.6	-09 53 26	62	1.1	< 9.5	—	0.96 ± 0.03
UGC2529	03 05 29.6	-00 22 54	64	1.2	< 9.8	—	0.93 ± 0.04
SDSSJ0805+06	08 05 37.7	+06 59 35	123	0.8	< 18.8	—	0.99 ± 0.01
SDSSJ0937+09	09 37 09.0	+09 27 51	71	0.8	< 10.9	—	0.93 ± 0.03
SDSSJ0950+11	09 50 11.2	+11 18 30	91	0.8	< 13.9	—	0.99 ± 0.01
2MASJ1011+07	10 11 09.4	+07 46 49	63	0.8	< 9.6	—	0.95 ± 0.03
2MASJ1014+07	10 14 58.9	+07 48 03	80	0.4	< 12.2	—	0.97 ± 0.01
LEDA31382	10 35 42.3	+05 36 58	76	0.5	< 11.6	—	0.93 ± 0.03
SDSSJ1104+05	11 04 14.6	+05 07 37	91	1.0	< 13.9	—	0.99 ± 0.01
2MASJ1110+04	11 10 37.4	+04 11 29	67	0.5	< 10.3	—	0.99 ± 0.01
SDSSJ1112+09	11 12 50.2	+09 31 39	60	1.5	< 9.2	—	0.96 ± 0.02
IC3069	12 16 19.9	+10 09 39	52	1.6	< 7.9	—	0.98 ± 0.01
SDSSJ1328-02	13 28 46.9	-02 02 28	160	0.5	< 24.5	—	0.97 ± 0.02
UGC09359	14 33 15.8	-01 08 24	76	1.0	< 11.6	—	0.93 ± 0.05
CGCG050-042	15 36 46.6	+07 50 01	270	0.3	< 41.3	—	0.98 ± 0.02
UGC10005	15 45 14.4	+00 46 20	90	1.4	< 13.8	—	0.89 ± 0.05

Table B3. Derived parameters of the ALLSMOG sample. Column (1): Source name from NED. Column (2): Luminosity of the CO(2–1) emission line. Column (3): Molecular hydrogen mass, calculated assuming a constant α_{CO} appropriate for the Milky-Way. Column (4): Molecular hydrogen mass, calculated assuming a metallicity-dependent α_{CO} , as described in the text. Column (5): Atomic hydrogen mass. Column (6): Stellar mass, calculated from SDSS. Column (7): Gas-phase metallicity, calculated as described in the text. Column (8): Log star formation rate, from SDSS.

(1) Name	(2) $L'_{\text{CO}(2-1)}$ [10^8 K km/s pc 2]	(3) $\log M(\text{H}_2)^{\alpha=\text{const}}$ [M_{\odot}]	(4) $\log M(\text{H}_2)^{\alpha=f(Z)}$ [M_{\odot}]	(5) $\log M(\text{H I})$ [M_{\odot}]	(6) $\log M^*$ [M_{\odot}]	(7) Metallicity [$12+\log(\text{O}/\text{H})$]	(8) $\log \text{SFR}$ [M_{\odot}/yr]
<i>Detected sources:</i>							
IC0159	0.76 ± 0.12	8.53 ± 0.07	8.38 ± 0.07	9.55	9.70	8.89	0.23
UGC2004	6.43 ± 0.67	9.46 ± 0.04	9.23 ± 0.04	9.83	9.61	9.15	0.36
NGC1234	0.33 ± 0.07	8.18 ± 0.09	7.99 ± 0.09	9.67	9.58	8.98	0.21
2MASJ0839+03	2.33 ± 0.54	9.02 ± 0.09	8.81 ± 0.09	—	9.94	9.08	0.58
2MASJ0846+02	2.77 ± 0.47	9.09 ± 0.07	8.90 ± 0.07	—	9.84	8.99	0.09
2MASJ0855+03	2.49 ± 1.47	9.05 ± 0.20	8.94 ± 0.20	—	9.73	8.81	0.06
2MASJ0858+03	1.30 ± 0.46	8.76 ± 0.13	8.55 ± 0.13	—	9.80	9.08	0.11
2MASJ0910+07	3.64 ± 0.73	9.21 ± 0.08	8.99 ± 0.08	9.43	9.85	9.11	0.07
UGC4977	2.94 ± 0.47	9.12 ± 0.07	8.94 ± 0.07	—	9.91	8.95	0.19
MCG00-25-005	1.39 ± 0.26	8.79 ± 0.07	8.60 ± 0.07	10.1	9.70	9.01	0.02
NGC2936	26.0 ± 0.69	10.0 ± 0.01	9.83 ± 0.01	—	8.53	9.17	0.34
2MASJ0939+06	2.07 ± 0.37	8.96 ± 0.07	8.92 ± 0.07	9.81	9.44	8.71	0.33
IC0605	2.12 ± 0.35	8.98 ± 0.07	8.79 ± 0.07	9.93	9.89	8.97	0.23
UGC5648	1.92 ± 0.42	8.93 ± 0.08	8.72 ± 0.08	10.1	9.99	9.08	0.02
NGC3436	1.25 ± 0.25	8.75 ± 0.08	8.60 ± 0.08	9.77	9.64	8.89	0.05
MCG00-29-013	3.21 ± 0.54	9.16 ± 0.07	8.95 ± 0.07	9.66	9.98	9.07	0.15
UGC6329	0.86 ± 0.21	8.58 ± 0.10	8.40 ± 0.10	10.0	9.80	8.98	0.02
UGC06838	0.13 ± 0.05	7.78 ± 0.15	7.62 ± 0.15	9.59	9.32	8.91	0.33
MCG00-34-038	4.44 ± 0.43	9.30 ± 0.04	9.08 ± 0.04	9.96	9.91	9.09	0.14
CGCG017	1.53 ± 0.27	8.83 ± 0.08	8.61 ± 0.08	10.0	9.96	9.12	−0.79
UGC085276	0.84 ± 0.12	8.57 ± 0.07	8.38 ± 0.07	9.31	9.68	9.01	−0.44
NGC5405	1.40 ± 0.27	8.80 ± 0.08	8.60 ± 0.08	10.1	9.98	9.03	0.27
NGC5414	1.24 ± 0.22	8.74 ± 0.07	8.58 ± 0.07	9.79	9.74	8.92	0.25
UGC11631	0.72 ± 0.06	8.51 ± 0.04	8.41 ± 0.04	9.72	9.57	8.80	0.59
2MASJ2235−08	1.74 ± 0.21	8.89 ± 0.05	8.70 ± 0.05	9.75	9.78	9.00	0.25
<i>Non-detected sources:</i>							
UGC00272	< 0.22	< 7.85	< 7.81	9.69	9.36	8.91	0.21
KUG0200	< 0.18	< 7.96	< 7.93	9.63	9.11	8.61	0.92
UGC2529	< 0.70	< 8.43	< 8.44	10.1	9.42	8.74	0.02
SDSSJ0805+06	< 0.48	< 8.33	< 8.32	9.18	8.62	8.66	−1.25
SDSSJ0937+09	< 0.64	< 8.47	< 8.44	9.77	8.75	8.64	−0.82
SDSSJ0950+11	< 0.54	< 8.43	< 8.41	8.80	8.57	8.61	−0.88
2MASJ1011+07	< 0.75	< 8.40	< 8.38	9.83	9.96	8.85	0.11
2MASJ1014+07	< 1.09	< 8.56	< 8.54	9.74	9.51	8.84	0.00
LEDA31382	< 1.00	< 8.52	< 8.50	9.95	9.95	8.85	0.08
SDSSJ1104+05	< 0.47	< 8.46	< 8.41	8.94	8.67	8.52	−1.04
2MASJ1110+04	< 0.94	< 8.52	< 8.51	9.73	9.51	8.80	0.56
SDSSJ1112+09	< 0.45	< 8.36	< 8.32	9.35	8.89	8.60	−0.85
IC3069	< 0.33	< 8.23	< 8.20	9.32	8.99	8.60	−0.51
SDSSJ1328−02	< 0.43	< 8.09	< 8.02	9.63	8.82	9.00	−0.50
UGC09359	< 0.26	< 8.07	< 8.07	9.58	8.96	8.65	0.17
CGCG050-042	< 0.57	< 8.51	< 8.47	9.03	8.54	8.55	−1.44
UGC10005	< 0.28	< 8.00	< 7.97	9.45	9.06	8.79	1.08

APPENDIX C: MAPS AND SPECTRA

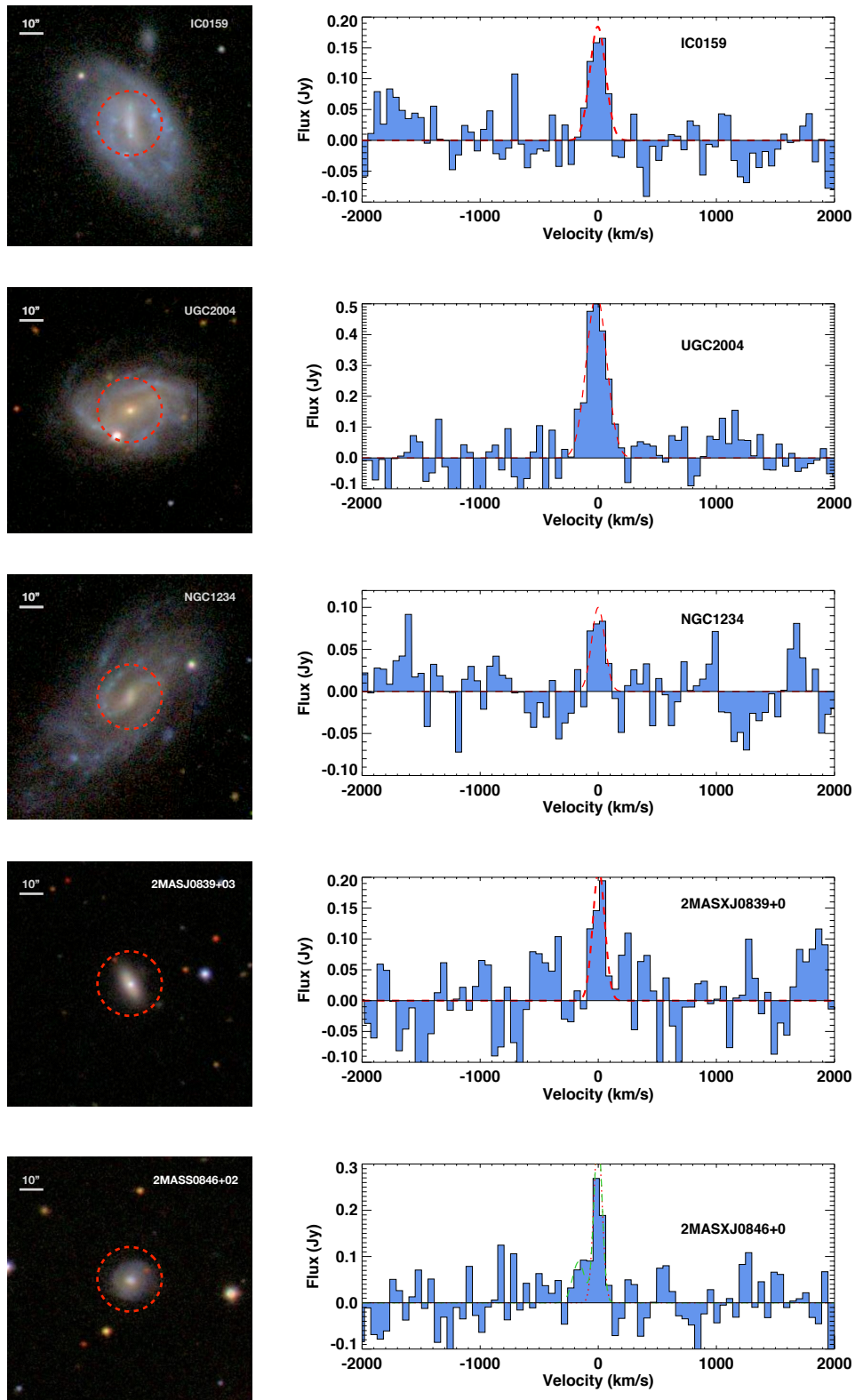


Figure C1. SDSS cutout images of galaxies in the ALLSMOG sample detected in CO(2 – 1) emission, and their corresponding spectra. Galaxies are shown at a constant size scale (10'' is shown inset in the upper left). In each left hand panel, the central circle shows the size of the 27'' APEX beam. Spectra are presented at 60 km s⁻¹ resolution, and overlaid with the best fitting Gaussian profile.

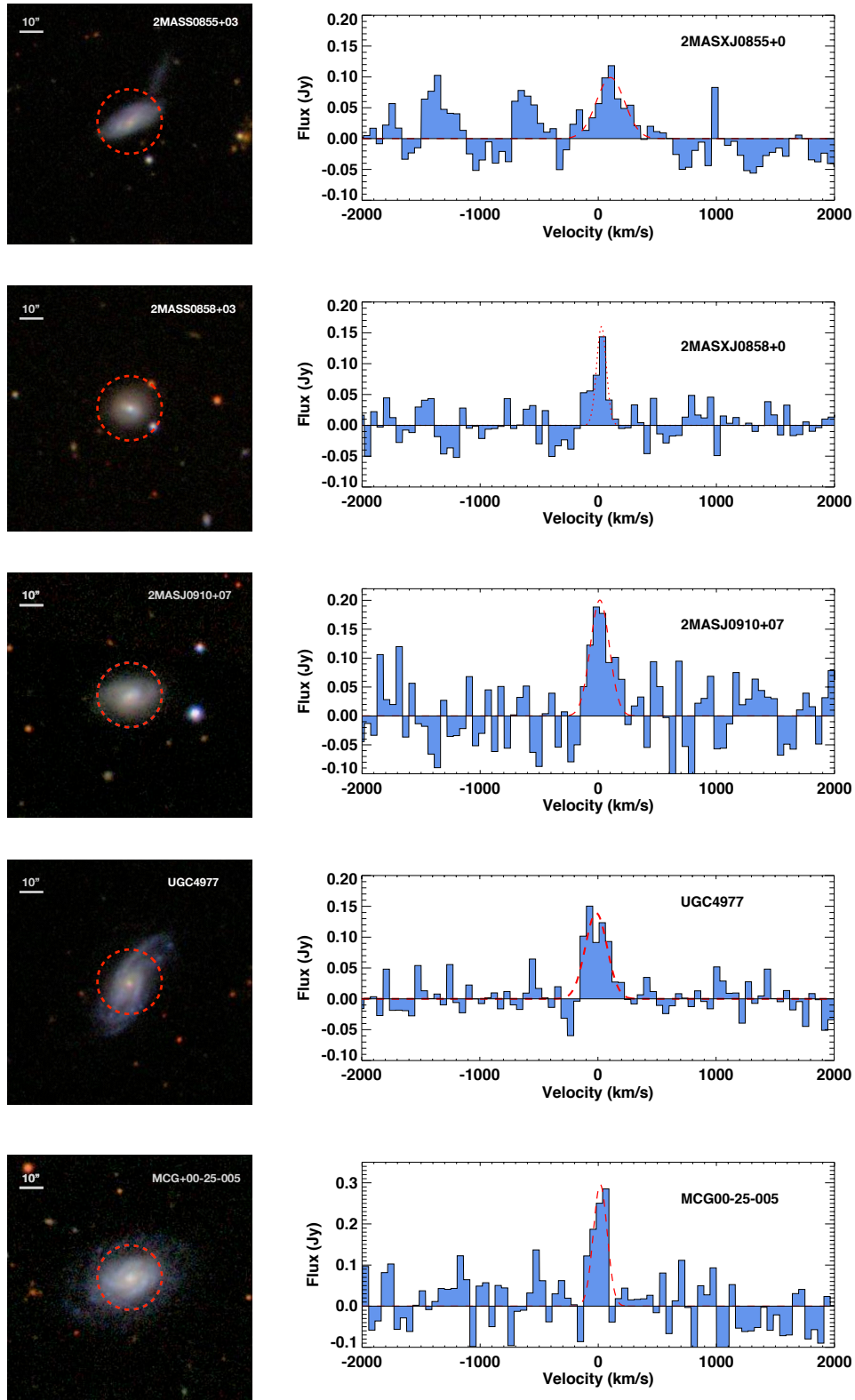


Figure C2. Panels are the same as Fig. C1. The galaxy MCG+00-27-013 exhibits a double-peaked spectrum, and has been fitted with both a single and a double Gaussian profile (as discussed in the text).

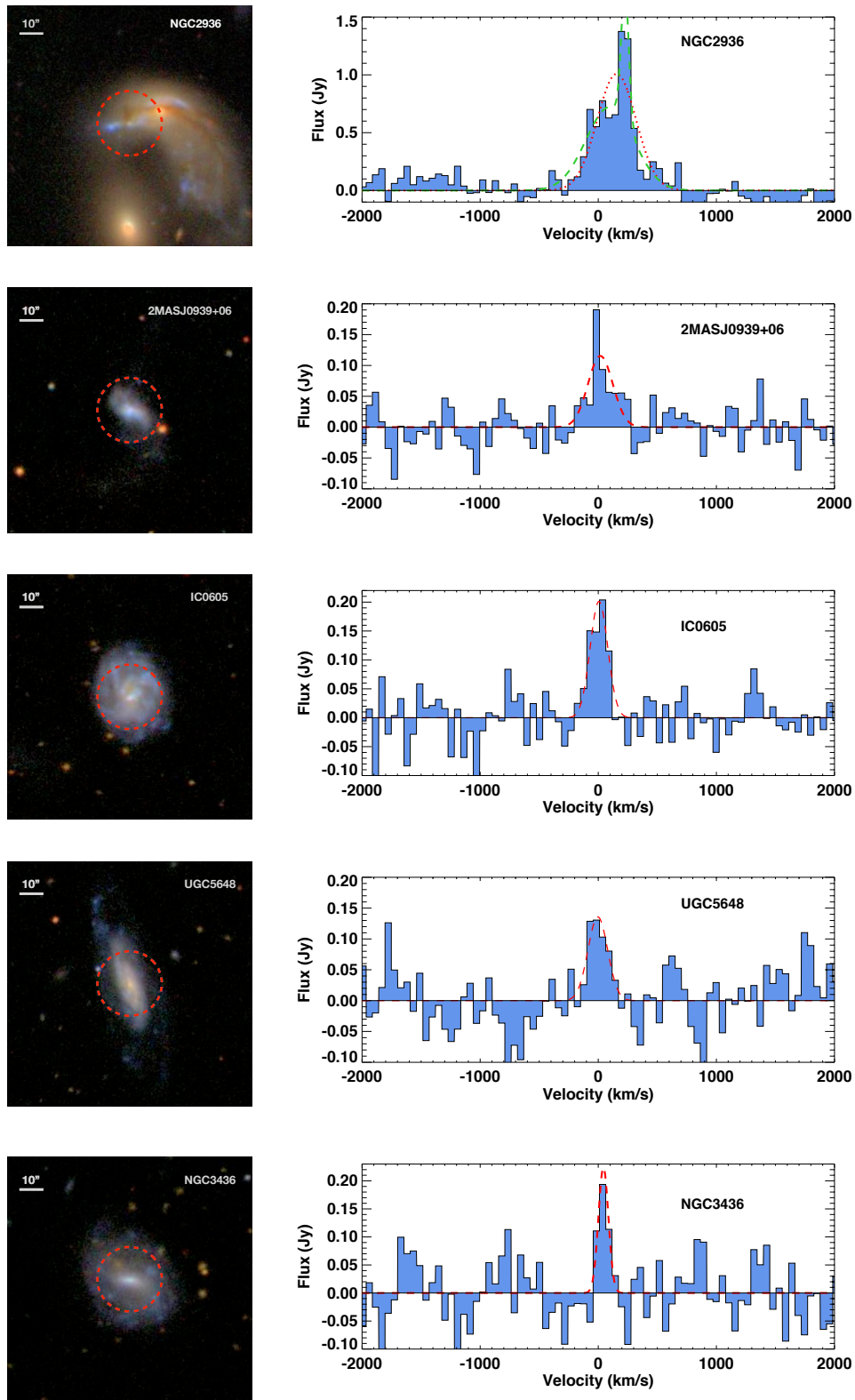


Figure C3. Panels are the same as Fig. C1. The galaxy UGC06838 has been presented at higher spectral resolution (20 km s^{-1} channels) due to the narrow linewidth.

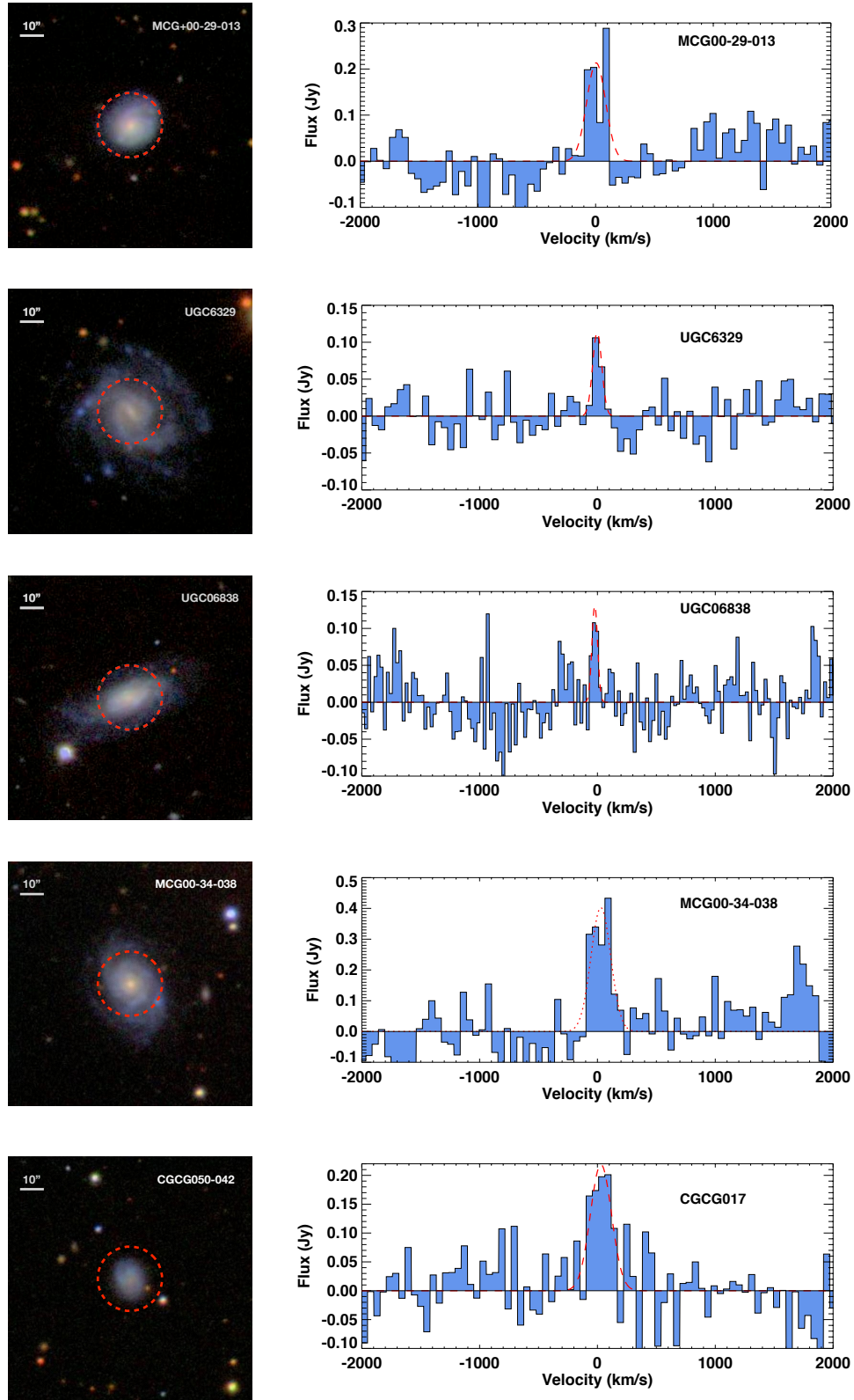


Figure C4. Panels are the same as Fig. C1.

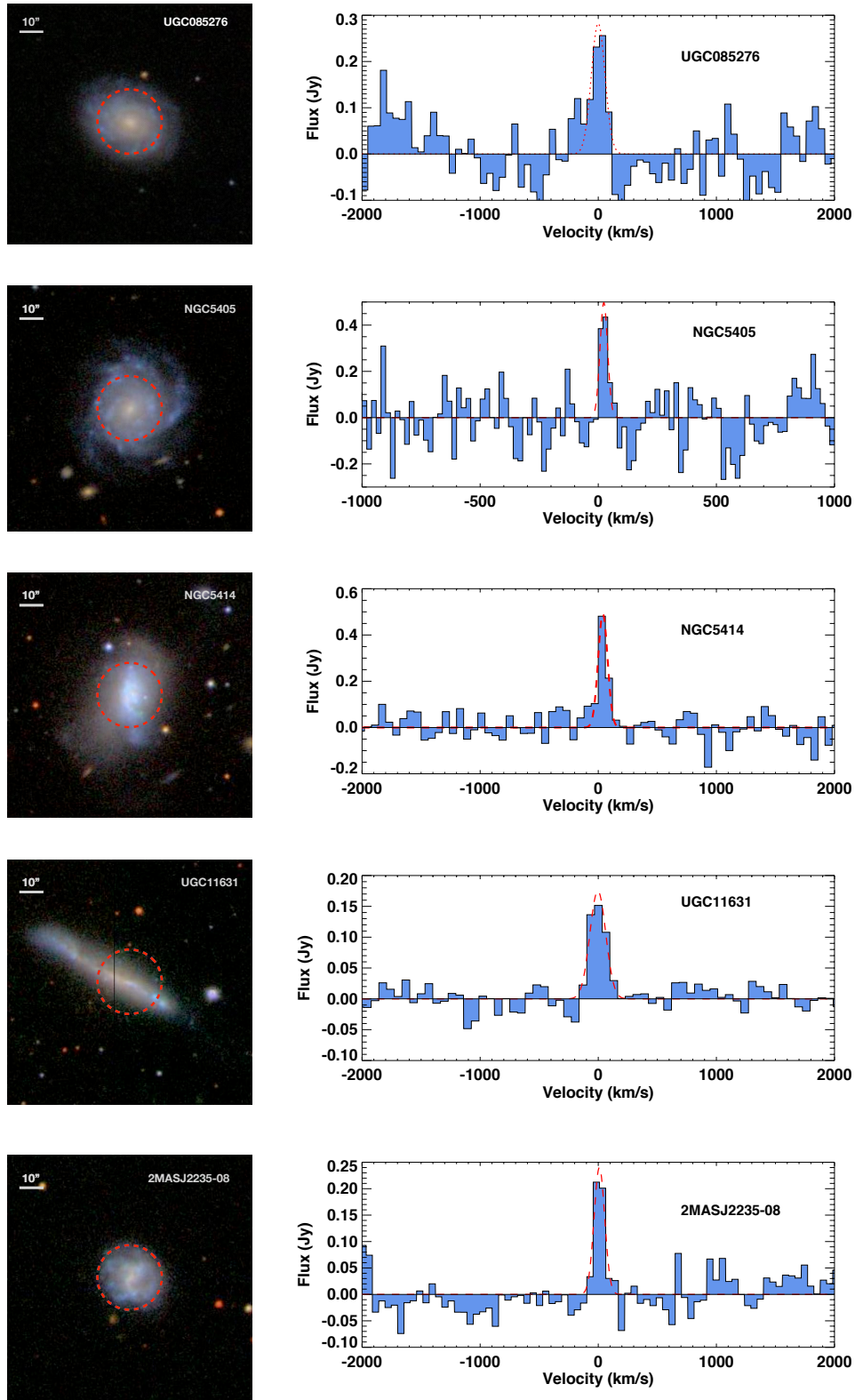


Figure C5. Panels are the same as Fig. C1.

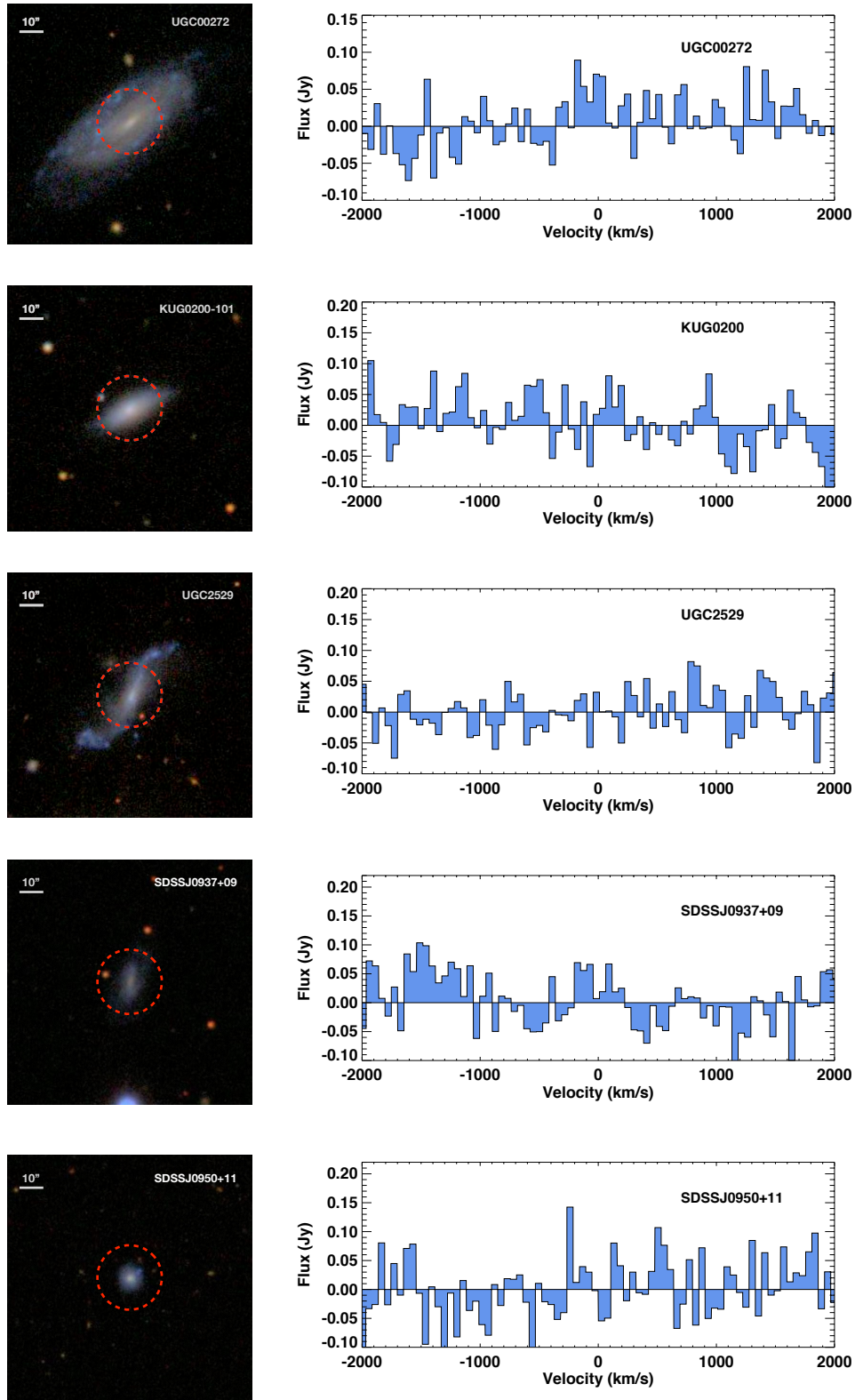


Figure C6. SDSS cutout images of galaxies in the ALLSMOG sample **not** detected in CO(2 – 1) emission, and their corresponding spectra. Galaxies are shown at a constant size scale (10'' is shown inset in the upper left). In each left hand panel, the central circle shows the size of the 27'' APEX beam. Spectra are presented at 60 km s⁻¹ resolution.

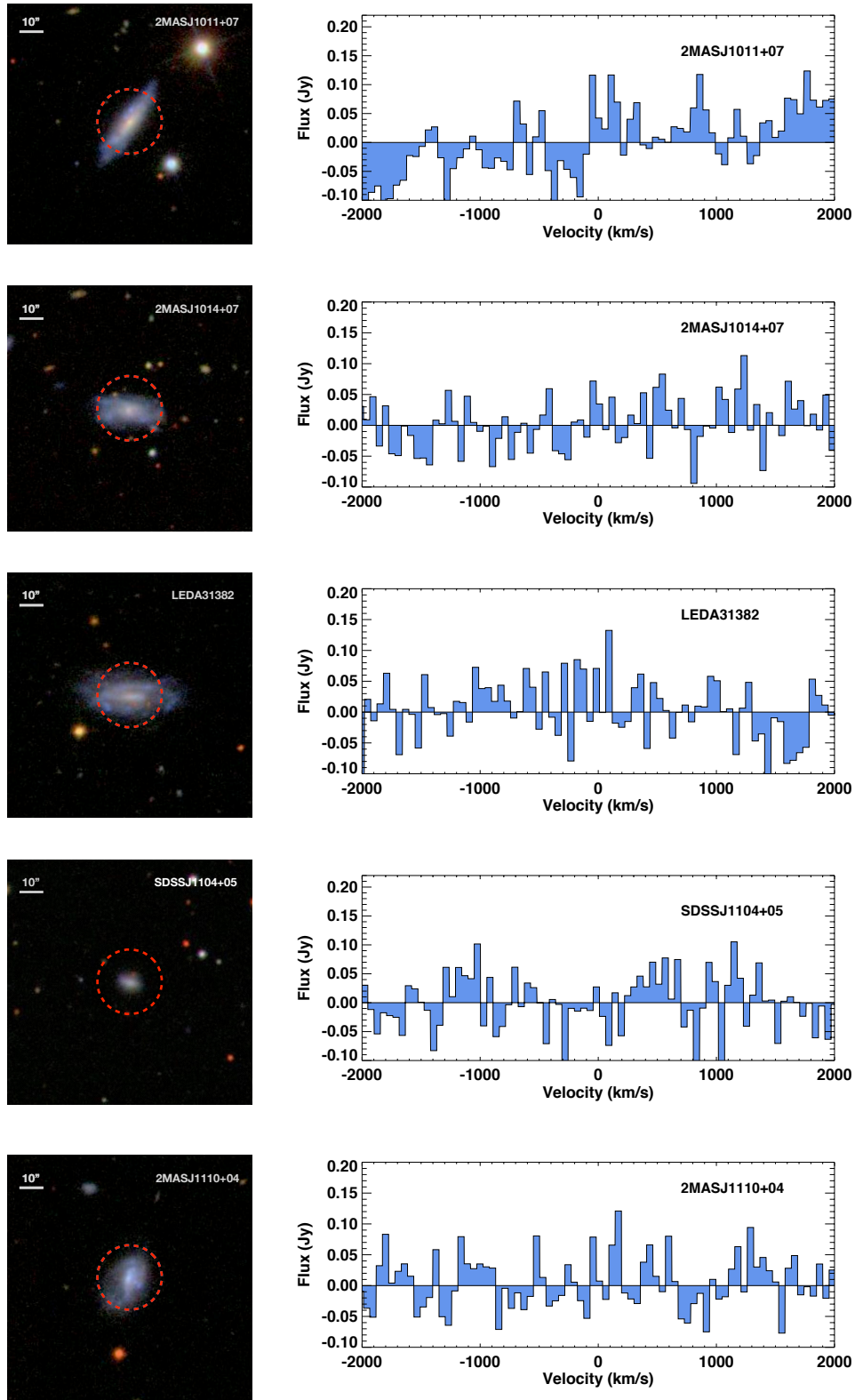


Figure C7. Panels are the same as Fig. C6.

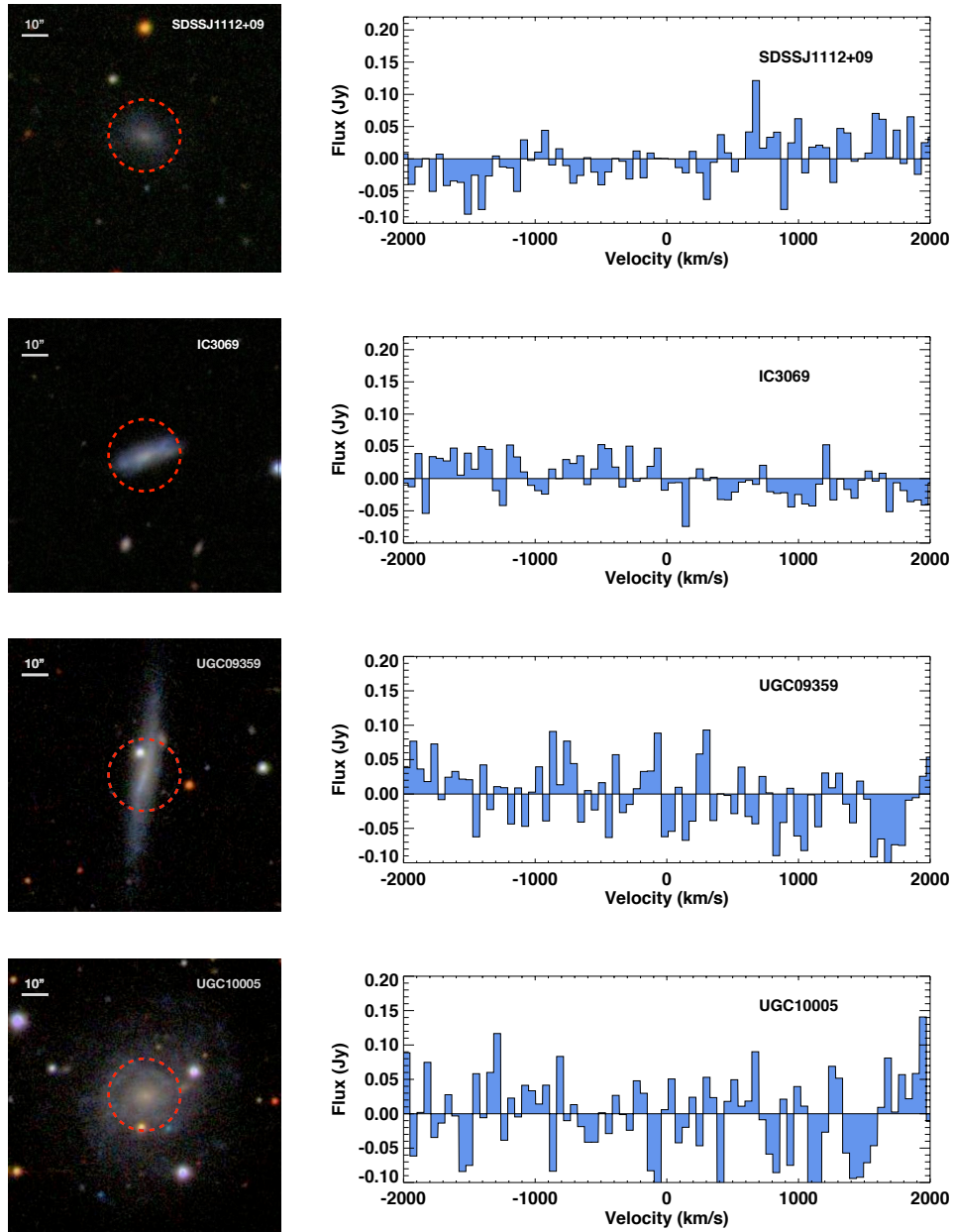


Figure C8. Panels are the same as Fig. C6.